NASA/CR—2003-212195

Glenn-HT/BEM Conjugate Heat Transfer Solver for Large-Scale Turbomachinery Models

E. Divo, E. Steinthorsson, F. Rodriguez, A.J. Kassab and J.S. Kapat
University of Central Florida, Orlando, Florida

April 2003

The NASA STI Program Office . . . in Profile

Since its founding, NASA has been dedicated to the advancement of aeronautics and space science. The NASA Scientific and Technical Information (STI) Program Office plays a key part in helping NASA maintain this important role.

The NASA STI Program Office is operated by Langley Research Center, the Lead Center for NASA's scientific and technical information. The NASA STI Program Office provides access to the NASA STI Database, the largest collection of aeronautical and space science STI in the world. The Program Office is also NASA's institutional mechanism for disseminating the results of its research and development activities. These results are published by NASA in the NASA STI Report Series, which includes the following report types:

- TECHNICAL PUBLICATION. Reports of completed research or a major significant phase of research that present the results of NASA programs and include extensive data or theoretical analysis. Includes compilations of significant scientific and technical data and information deemed to be of continuing reference value. NASA's counterpart of peer-reviewed formal professional papers but has less stringent limitations on manuscript length and extent of graphic presentations.

- TECHNICAL MEMORANDUM. Scientific and technical findings that are preliminary or of specialized interest, e.g., quick release reports, working papers, and bibliographies that contain minimal annotation. Does not contain extensive analysis.

- CONTRACTOR REPORT. Scientific and technical findings by NASA-sponsored contractors and grantees.

- CONFERENCE PUBLICATION. Collected papers from scientific and technical conferences, symposia, seminars, or other meetings sponsored or cosponsored by NASA.

- SPECIAL PUBLICATION. Scientific, technical, or historical information from NASA programs, projects, and missions, often concerned with subjects having substantial public interest.

- TECHNICAL TRANSLATION. English-language translations of foreign scientific and technical material pertinent to NASA's mission.

Specialized services that complement the STI Program Office's diverse offerings include creating custom thesauri, building customized databases, organizing and publishing research results . . . even providing videos.

For more information about the NASA STI Program Office, see the following:

- Access the NASA STI Program Home Page at ***http://www.sti.nasa.gov***

- E-mail your question via the Internet to help@sti.nasa.gov

- Fax your question to the NASA Access Help Desk at 301–621–0134

- Telephone the NASA Access Help Desk at 301–621–0390

- Write to:
  NASA Access Help Desk
  NASA Center for AeroSpace Information
  7121 Standard Drive
  Hanover, MD 21076

NASA/CR—2003-212195

Glenn-HT/BEM Conjugate Heat Transfer Solver for Large-Scale Turbomachinery Models

E. Divo, E. Steinthorsson, F. Rodriguez, A.J. Kassab and J.S. Kapat
University of Central Florida, Orlando, Florida

Prepared under Grant NAG3–2691

National Aeronautics and
Space Administration

Glenn Research Center

April 2003

This report contains preliminary findings, subject to revision as analysis proceeds.

The Propulsion and Power Program at
NASA Glenn Research Center sponsored this work.

Available from

NASA Center for Aerospace Information
7121 Standard Drive
Hanover, MD 21076

National Technical Information Service
5285 Port Royal Road
Springfield, VA 22100

Available electronically at http://gltrs.grc.nasa.gov

Abstract

We report on progress in the development and application of a coupled Boundary Element/Finite Volume Method temperature-forward/flux-back algorithm developed to solve conjugate heat transfer arising in 3-D film-cooled turbine blades. Here, heat conduction within the blade is coupled to heat transfer in the external fluid flow field that is convecting heat into/or out of the blade. In the BEM formulation no interior mesh is generated and the surface heat flux is computed in the solution. We adopt a loosely coupled strategy where each set of field equations, Navier-Stokes for the external field and heat conduction for the internal field, is solved to provide boundary conditions for the other. The equations are solved in turn until iterative convergence criteria requiring continuity of temperature and heat flux are met at the fluid-solid interface. The NASA-Glenn turbomachinery Navier-Stokes code Glenn-HT is coupled to a 3-D BEM steady state heat conduction solver. Glenn-HT is a multi-block cell-centered finite volume explicit code using a multi-stage Runge-Kutta based multigrid method time marching. The steady-state solution is sought by marching in time until dependent variables reach their steady-state values. The steady heat conduction equation is solved using the BEM with isoparametric bilinear discontinuous elements. We choose to employ discontinuous elements as they provide high levels of accuracy in computed heat flux values without resorting to special treatment of corner points required by continuous elements particularly when first kind boundary conditions are imposed to the conduction solver as is the case in the algorithm adopted in this paper. Moreover, the use of discontinuous elements throughout the BEM model eliminates much of the overhead associated with continuous elements, in particular, there is no need to generate, store, or access a connectivity matrix when using discontinuous elements. Details of the interpolation used to exchange nodal temperature and flux information from the disparate CFD and BEM grids are discussed. Results from a CHT numerical simulation of a 3-D film-cooled blade section are presented and are compared with those obtained from the standard approach of

a two temperature model. A significant difference in the level and distribution of the metal temperatures is found between the two models.

Finally, current developments of an iterative strategy accommodating large numbers of unknowns by an artificial subsectioning of the blade are presented. The blade is subsectioned in the spanwise direction and a specially tailored iterative scheme is developed to solve the conduction problem with each subsection BEM problem solved using a direct LU solver. An adiabatic intial guess may be made for the sub-structure interface BEM nodes. Although the iterative method converges in some cases the iteration may be slow to converge. A better initial guess is provided via a physically-based initialization of the substructure interfacial temperatures. This is shown to provide an effective starting point for the iterative algorithm and significantly reduce the number of iterations required to achieve convergence. Results from several simulations in 2-D and 3-D show the process converges efficiently and offers substantial computational and storage savings.

1 Introduction

Engineering analysis of complex mechanical devices such as turbomachines requires ever-increasing fidelity in numerical models upon which designers rely in their efforts to attain demanding specifications placed on efficiency and durability of modern machinery. Consequently, the trend in computational mechanics is to adopt coupled-field analysis to obtain computational models which attempt to better mimic the physics under consideration, see Kassab and Aliabadi [1]. The coupled field problem which we address in this paper is conjugate heat transfer (CHT): the coupling of convective heat transfer external to the solid body of a thermal component coupled to conduction heat transfer within the solid body of that component, see Figure 1. Conjugate heat transfer thus applies to any thermal system in which multi-mode convective/conduction heat transfer is of particular importance to thermal design, and thus CHT arises naturally in most instances where external and internal temperature fields are coupled.

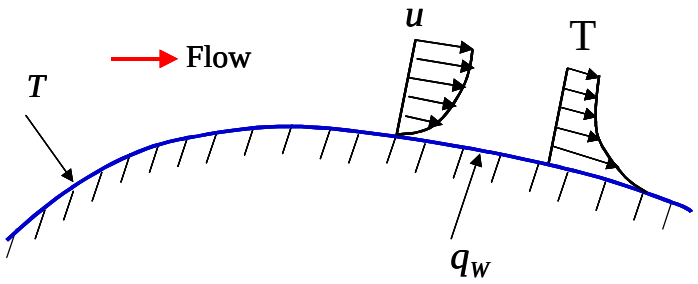

Figure 1. CHT problem: external convective heat transfer coupled to heat conduction within the solid.

Conjugacy is often ignored in most analytical solutions and numerical simulations. For instance, it is common practice in analysis of turbomachinery, Heidmann et al. [2], to carry out separate flow and heat conduction analyses. Heat transfer coefficient as well as film effectiveness values are predicted using two independent external flow solutions each computed by imposing a different constant wall temperature at the surfaces of the turbine blade exposed to hot gases and film cooling air. The film effectiveness determines the reference temperature for the computed film coefficients. In turn, these values are used to impose convective boundary conditions to a

conduction solver to obtain predicted metal temperatures. As will be shown in the example section of this paper, the shortcomings of this approach which neglects the effects of the wall temperature distribution on the development of the thermal boundary layer are readily overcome by a CHT analysis in which the coupled nature of the field problem is explicitly taken into account in the analysis.

There are two basic approaches to solving coupled field problems. In the first approach, a direct coupling is implemented in which different fields are solved simultaneously in one large set of equations. Direct coupling is mostly applicable for problems where time accuracy is critical, for instance, in aero-elasticity applications where the time scale of the fluid motion is on the same order as the structural modal frequency. However, this approach suffers from a major disadvantage due to the mismatch in the structure of the coefficient matrices arising from BEM, FEM and/or FVM solvers. That is, given the fully populated nature of the BEM coefficient matrix, the direct coupling approach would severely degrade numerical efficiency of the solution by directly incorporating the fully populated BEM equations into the sparsely banded FEM or FVM equations. A second approach which may be followed is a loose coupling strategy where each set of field equations is solved separately to produce boundary conditions for the other. The equations are solved in turn until an iterated convergence criterion, namely continuity of temperature and heat flux, is met at the fluid-solid interface. The loose coupling strategy is particularly attractive when coupling auxiliary field equations to computational fluid dynamics codes as the structure of neither solver interferes in the solution process.

Several approaches can be taken to solve coupled field problems and most are based on either finite elements (FEM) or finite volume methods (FVM), or a combination of these two field solvers. Examples of such loosely coupled approaches applied to a variety of CHT problems ranging from engine block models to turbomachinery can be found in Comini et al. [3], Shyy and Burke [4], Patankar [5], Kao and Liou [6], Hahn et al. [7], Bohn et al. [8,9], and in Tayla et al. [10] where multi-disciplinary optimization is considered for CHT modeled turbine airfoil designs. Hassan et al. [11] develop a conjugate algorithm which loosely couples a FVM-based

Hypersonic CFD code to an FEM heat conduction solver in an effort to predict ablation profiles in hypersonic re-entry vehicles. Here, the structured grid of the flow solver is interfaced with the un-structured grid of heat conduction solvers in a quasi-transient CHT solution tracing the re-entry vehicle trajectory. Issues in loosely coupled analysis of the elastic response of solid structures perturbed by external flowfields arising in aero-elastic problems can be found in Brown [12] and Dowell and Hall [13]. In either case, the coupled field solution requires complete meshing of both fluid and solid regions while enforcing solid/fluid interface continuity of fluxes and temperatures, in the case of CHT analysis, or displacement and traction, in the case of aero-elasticity analysis.

A different approach taken by Li and Kassab [14,15] and Ye et al. [16] who develop a BEM-based CHT algorithm thereby avoiding meshing of the solid region for the conduction solution. The method couples the boundary element method (BEM) to a FVM Navier-Stokes solver and was applied to solving two-dimensional steady state compressible subsonic CHT problems over cooled and uncooled turbine blades. The conduction problem requires solution of the Laplace equation for the temperature (or the Kirchhoff transform in the case of temperature dependent conductivity), and, as such, only requires a boundary discretization thereby eliminating the onerous task of grid generation within intricate regions of the solid. The boundary discretization utilized to generate the computational grid for the external flow-field can be considerably coarsened to provide the boundary discretization required for the boundary element method. Most modern grid generators used in computational fluid dynamics, for instance, GridPro^{TM} [17], the topology-based algebraic grid generator used in the examples presented in this paper, allow for the multigrid option. Several levels of coarse discretization can thus be readily obtained. Furthermore, the BEM/FVM method offers the additional advantage of providing heat flux values and this stems from the fact that nodal unknowns which appear in the BEM are the surface temperatures and heat fluxes. Consequently, solid/fluid interfacial heat fluxes which are required to enforce continuity in CHT problems are naturally provided by the BEM conduction analysis. This is in sharp contrast to domain meshing methods such as FVM

and FEM where heat fluxes are computed by numerical differentiation in a post-processing stage. He et al. [18,19] adopted the BEM/FVM approach in further studies of CHT in incompressible flow in ducts subjected to constant wall temperature and constant heat flux boundary conditions. Kontinos [20] also adopted the BEM/FVM coupling algorithm to solve the CHT over metallic thermal protection panels at the leading edge of the X-33 in a Mach 15 hypersonic flow regime. Rahaim and Kassab [21] and Rahaim et al. [22] adopt a BEM/FVM strategy to solve time-accurate CHT problems for supersonic compressible flow over a 2-D wedged, and they present experimental validation of this CHT solver. In their studies, the dual reciprocity BEM [23] was used for transient heat conduction, while a cell-centered FVM was chosen to resolve the compressible turbulent Navier-Stokes equations.

In this paper, we report on progress in the development and application of a BEM-based temperature forward/flux back (TFFB) coupling algorithm developed to solve conjugate heat transfer (CHT) arising in 3-D film-cooled turbine blades. The NASA-Glenn turbomachinery Navier-Stokes code Glenn-HT is coupled to a 3-D BEM steady state heat conduction solver[24,25]. The steady-state solution is sought by marching in time until dependent variables reach their steady-state values, and, as such, intermediate temporal solutions are not physically meaningful. In this mode of solving the steady-state problem, time-marching can be viewed as a relaxation scheme, and local time-stepping and implicit residual smoothing are used to accelerate convergence. The steady heat conduction equation reduces to the Laplace equation, and it is solved using the BEM with isoparametric bilinear discontinuous elements. We choose to employ discontinuous elements as they provide high levels of accuracy in computed heat flux values especially at sharp corners regions where first kind boundary conditions are imposed without resorting to special treatment of corner points required by continuous elements in particular when first kind boundary conditions are imposed [26,27]. In this application, sharp corners occur in many locations and first kind boundary conditions are imposed on all metal surfaces. Moreover, the use of discontinuous elements throughout the BEM model eliminates much of the overhead

associated with continuous elements, in particular, there is no need to generate, store, or access a connectivity matrix when using discontinuous elements.

In order to resolve the flow physics, the CFD grid must be clustered in many regions. The BEM grid does not require such fine clustering and consequently the two grids are of quite different coarseness. The details of the interpolation used to exchange nodal temperature and flux information from the disparate CFD and BEM grids are presented. Results from a CHT numerical simulation of a 3-D film-cooled blade section are presented and results are compared with those obtained from the standard approach of a two temperature model. Significant difference in the level and distribution of the metal temperature is found between the two-temperature and CHT models. Finally, in order to address the large number of unknowns appearing in the 3-D BEM model, current developments of a strategy of artificial subsectioning of the blade are presented. Here, the approach is to subsection the blade in the spanwise direction. A specially tailored iterative scheme is developed to solve the conduction problem with each subsection BEM problem solved using a direct LU solver. A physically based initial guess is used to provide a good starting point for the iterative algorithm. Results from 2-D and 3-D simulations show the process converges efficiently and offers substantial computational and storage savings.

2 Governing Equations

We first present the governing equations for the coupled field problem under consideration. The CHT problems arising in turbomachinery involves external flow fields that are generally compressible and turbulent, and these are governed by the compressible Navier-Stokes equations supplemented by a turbulence model. Heat transfer within the blade is governed by the heat conduction equation. Linear as well as non-linear options are considered. However, fluid flows within internal structures to the blade, such as film cooling holes and channels, are usually low-speed and incompressible. Consequently, density-based compressible codes tend to experience numerical difficulties in modeling such flows, unless low Mach number pre-

conditioning is implemented, see Turkel [28,29]. The Glenn-HT code is specialized to turbomachinery applications for which air is the working fluid and which is modeled as an ideal gas.

2.1 Governing Equations for The Flow Field

The governing equations for the flow field are the compressible Navier-Stokes equations, which describe the conservation of mass, momentum and energy. These can be written in integral form as

$$\int_{\Omega} \frac{\partial \underset{\sim}{W}}{\partial t} d\Omega + \int_{\Gamma} \left(\underset{\sim}{F} - \underset{\sim}{T} \right) \cdot \widehat{n} d\Gamma = \int_{\Omega} \underset{\sim}{S} d\Omega \tag{1}$$

where Ω denotes the volume, Γ denotes the surface bounded by the volume Ω, and $\widehat{n}$ is the outward-drawn normal. The conserved variables are contained in the vector $\underset{\sim}{W} = (\rho,\ \rho u,\ \rho v,\ \rho w,\ \rho e,\ \rho k,\ \rho\omega)$, where, $\rho,\ u,\ v,\ w,\ e,\ k, \omega$ are the density, the velocity components in x-, y-, and z-directions, and the specific total energy. The kinetic energy of turbulent fluctuations is denoted by k and the specific dissipation rate ω appear in the two equation k-ω Wilcox turbulence model [30, 31] with modifications by Menter [32] and Chima [33] as implemented in Glenn-HT. The vectors $\underset{\sim}{F}$ and $\underset{\sim}{T}$ are convective and diffusive fluxes respectively, $\underset{\sim}{S}$ is a vector containing all terms arising from the use of a non-inertial reference frame as well as production and dissipation of turbulent quantities. The working fluid is air, and it is modeled as an ideal gas. A rotating frame of reference can be adopted for modeling of rotating flows. The effective viscosity is given by

$$\mu = \mu_l + \mu_t \tag{2}$$

where $\mu_t = \rho k/\omega$. The thermal conductivity of the fluid is then computed by a Prandtl number analogy where

$$k_f = \frac{\gamma}{\gamma - 1} \left[\frac{\mu_l}{Pr_l} + \frac{\mu_t}{Pr_t} \right] \tag{3}$$

and Pr is the Prandtl number and γ is the specific heat ratio. The subscripts l and t refers to laminar and turbulent values respectively.

2.2 The Governing Equations of the Heat Conduction Field

In the steady-state CHT solutions obtained in this paper, the NS equations are solved to steady state by a time marching scheme converging towards steady-state. A steady heat conduction analysis is carried out using the BEM at each time level chosen for the external flow-field and internal conduction field to interact in the iterative process. As such, the governing equation under consideration is

$$\nabla \cdot [k(T_s)\nabla T_s] = 0 \tag{4}$$

where, T_s denotes the temperature of the solid, and k_s is the thermal conductivity of the solid material. If the thermal conductivity is taken as constant, then the above reduces to the Laplace equation for the temperature. When the thermal conductivity variation with temperature is an important concern, the nonlinearity in the steady-state heat conduction equation can readily be removed by introducing the classical Kirchhoff transform, $U(T),$ see [34-37], which is defined as

$$U(T)=\frac{1}{k_o}\int_{T_o}^{T} k_s(T)dT \tag{5}$$

where T_o is the reference temperature and k_o is the reference thermal conductivity. The transform and its inverse are readily evaluated, either analytically or numerically, and the heat conduction equation transforms to a Laplace equation for the transform parameter $U(T)$. The heat conduction equation thus reduces to the Laplace equation in any case, and this equation is readily solved by the BEM.

In the conjugate problem, continuity of temperature and heat flux at the blade surface, Γ, must be satisfied:

$$T_f = T_s$$
$$k_f \frac{\partial T_f}{\partial n} = -k_s \frac{\partial T_s}{\partial n} \tag{6}$$

Here, T_f is the temperature computed from the N-S solution, T_s is the temperature within the solid which is computed from the BEM solution, and $\partial/\partial n$ denotes the normal derivative. Both first kind and second kind boundary conditions transform linearly in the case of temperature dependent conductivity. In such a case, the fluid temperature is used to evaluate the Kirchhoff transform and this is used a boundary condition of the first kind for the BEM conduction solution in the solid. Subsequently the computed heat flux, in terms of U, is scaled to provide the heat flux which is in turn used as an input boundary condition for the flow-field.

3 Field Solver Solution Algorithms

A brief description of the Glenn-HT code is given in this section. Details of the code and its verification in turbomachinery application can be found in [2, 38-41]. The heat conduction equation is solved using BEM.

3.1 Navier-Stokes Solver

Glenn-HT uses a cell-centered FVM to discretize the NS equations. Equation (1), is integrated over a hexahedral computational cell with the nodal unknowns located at the cell center (i, j, k). The convective flux vector is discretized by a central difference supplemented by artificial dissipation as described in Jameson et al. [42]. The artificial dissipation is a blend of first and third order differences with the third order term active everywhere except at shocks and locations of strong pressure gradients. The viscous terms are evaluated using central differences. The overall accuracy of the code is second order, Heidmann et al. [2]. The resulting finite volume equations can be written at every computational node as

$$V_{i,j,k} \frac{d\underset{\sim}{\overline{W}}_{i,j,k}}{dt} + \underset{\sim}{q}_{i,j,k} - \underset{\sim}{d}_{i,j,k} = \underset{\sim}{s}_{i,j,k} \tag{7}$$

where $\underset{\sim}{\bar{W}}_{i,j,k}$ is the cell-volume averaged vector of conserved variables, $\underset{\sim}{q}_{i,j,k}$ and $\underset{\sim}{d}_{i,j,k}$ are the net flux and dissipation for the finite volume obtained by surface integration of Eqn. (1), and $\underset{\sim}{s}_{i,j,k}$ is the net finite source term. The above is solved using a time marching scheme based on a fourth order explicit Runge-Kutta time stepping algorithm. The steady-state solution is sought by marching in time until the dependent variables reach their steady-state values, and, as such, intermediate temporal solutions are not physically meaningful. In this mode of solving the steady-state problem, time-marching can be viewed as a relaxation scheme, and local time-stepping and implicit residual smoothing are used to accelerate convergence. A multigrid option is available in the code. The code also adopts a multi-block strategy to model complex geometries associated with film-cooled blade problems. Here, locally structured grids blocks are generated into a globally unstructured assembly.

Glenn-HT adopts a k-ω turbulence model which integrates to the wall and does not require maintaining a specified distance from the wall as no wall functions are used. The computational grid is sufficiently fine near the wall to yield a y^+ value of less than 1.0 at the first grid point away from the wall. A constant value of 0.9 is taken for the turbulent Prandlt number in all heat transfer computations, while a constant value of 0.72 is used for the laminar Prandtl number. Moreover, the temperature variation of the laminar viscosity is taken as a 0.7 power law, see Schlichting [43], and c_p is taken as constant.

3.2 Heat Conduction Boundary Element Solution

The heat conduction equation reduces to the same governing Laplace equation in the temperature or the Kirchhoff transform. In the boundary element method this governing partial differential equation is converted into a boundary integral equation (BIE), see [44-46], as

$$C(\xi)\,T(\xi) + \oint_S T(x) q^*(x,\xi)\,dS(x) = \oint_S q(x) T^*(x,\xi)\,dS(x) \tag{8}$$

where $S(x)$ is the surface bounding the domain of interest, ξ is the source point, x is the field point, $q(x) = -k\partial T/\partial n$ is the heat flux, $T^*(x,\xi)$ is the so-called fundamental solution, and $q^*(x,\xi)$ is its normal derivative with $\partial/\partial n$ denoting the normal derivative with respect to the outward-drawn normal. The fundamental solution (or Green free space solution) is the response of the adjoint governing differential operator at any field point x due to a perturbation of a Dirac delta function acting at the source point ξ. In our case, since the steady state heat conduction equation is self-adjoint, we have

$$k\nabla^2 T^*(x,\xi) = -\delta(x,\xi) \tag{9}$$

Solution to this equation can be found by several means, see for instance Liggett and Liu [47], Morse and Feschbach [48], and Kellog [49], as

$$\begin{aligned} T^*(x,\xi) &= -\frac{1}{2\pi k} ln\, r(x,\xi) \qquad \text{in 2-D} \\ &= \frac{1}{4\pi k\, r(x,\xi)} \qquad \text{in 3-D} \end{aligned} \tag{10}$$

where $r(x,\xi)$ is the Euclidean distance from the source point ξ. The free term $C(\xi)$ can be shown analytically to be

$$C(\xi) = \oint_{S(x)} -k\,\frac{\partial T^*(x,\xi)}{\partial n} dS(x) \tag{11}$$

Moreover, introducing the definition of the fundamental solution in the above, it can be readily be determined that $C(\xi)$ is the internal angle (in degrees in 2-D and in steradians in 3-D) subtended at source point divided by 2π in 2-D and by 4π in 3-D when the source point ξ is on the boundary and takes on a value of one when the source point ξ is at the interior. Consequently, the free term takes on values $1 \geq C(\xi) \geq 0$. In the standard boundary element method, the BIE is discretized using two levels of discretization:

1. the surface S is discretized into a series of $j = 1, 2...N$ elements. This is traditionally accomplished using polynomial interpolation, bilinear and biquadratic being the most common. In general,

$$S = \sum_{j=1}^{N} \Delta S_j \tag{12}$$

and on each surface element ΔS_j the geometry is discretized using local shape functions $N^k(\eta, \zeta)$ in terms a homogeneous coordinates (η, ζ) which each take on values between $[-1, 1]$ as

$$\begin{aligned} x_j(\eta, \zeta) &= \sum_{k=1}^{NGE} N^k(\eta, \zeta) x_j^k \\ y_j(\eta, \zeta) &= \sum_{k=1}^{NGE} N^k(\eta, \zeta) y_j^k \\ z_j(\eta, \zeta) &= \sum_{k=1}^{NGE} N^k(\eta, \zeta) z_j^k \end{aligned} \tag{13}$$

Here, (x_j^k, y_j^k, z_j^k) denote the location of the $k = 1, 2...NGE$ boundary nodes used to define the boundary element j geometry.

2. the distribution of the temperature and heat flux is modeled on the surface. This is usually accomplished using polynomial interpolation as well. Common discretizations include: constant (where the mean value of T and q are taken on an element surface), bilinear, or biquadratic. In general,

$$\begin{aligned} T_j(\eta, \zeta) &= \sum_{k=1}^{NPE} M^k(\eta, \zeta) T_j^k \\ q_j(\eta, \zeta) &= \sum_{k=1}^{NPE} M^k(\eta, \zeta) q_j^k \end{aligned} \tag{14}$$

It is noted that the order of discretization of the temperature and heat flux need not be the same as that used for the geometry, leading to subparametric (lower order than that used for the geometry), isoparametric (same order than that used for the geometry), and superparametric (higher order than that used for the geometry) discretizations. Moreover, the temperature and heat flux are discretized using $k = 1, 2, ...NPE$

discrete nodal values whose location within the element j can be chosen to

(a) coincide with the location of the geometric nodes: continuous elements.

(b) be located offset from the geometric nodes: discontinuous elements.

We choose to employ bilinear discontinuous isoparametric elements as they provide high levels of accuracy in computed heat flux values especially at sharp corners regions where first kind boundary conditions are imposed without resorting to special treatment of corner points required by continuous elements [26,27]. In this type of boundary element, the field variables T and q are modeled with discontinuous bilinear shape functions across each element while the geometry is represented locally as continuous bilinear surfaces. Figure 2 below shows a typical bilinear isoparametric boundary element along with its transformed representation in the local coordinate η-ζ system.

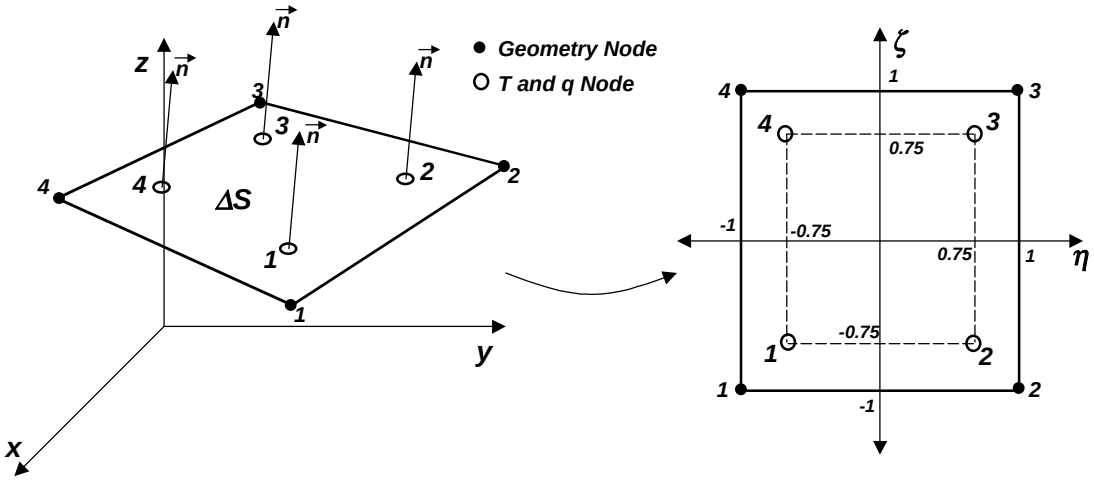

Figure 2. Bilinear isoparameteric discontinuous boundary element.

The global coordinate system (x, y, z) is transformed into a local coordinate system (η, ζ) by the backward transformation

$$x_j(\eta,\zeta) = \sum_{k=1}^{4} N^k(\eta,\zeta) x_j^k \tag{15}$$
$$y_j(\eta,\zeta) = \sum_{k=1}^{4} N^k(\eta,\zeta) y_j^k$$
$$z_j(\eta,\zeta) = \sum_{k=1}^{4} N^k(\eta,\zeta) z_j^k$$

where (x_j^k, y_j^k, z_j^k) are the global positions of the k-th geometric node of element j. The four bilinear shape functions are defined as

$$\begin{aligned} N^1(\eta,\zeta) &= \frac{1}{4}(1-\eta)(1-\zeta) \\ N^2(\eta,\zeta) &= \frac{1}{4}(1+\eta)(1-\zeta) \\ N^3(\eta,\zeta) &= \frac{1}{4}(1+\eta)(1+\zeta) \\ N^4(\eta,\zeta) &= \frac{1}{4}(1-\eta)(1+\zeta) \end{aligned} \tag{16}$$

The field variables, T and q, are modeled to vary bilinearly across the boundary element through the use of four discontinuous shape functions with nodes located at an off-set position of 12.5% from the edges of the element. The field variables and shape functions are described as follows:

$$T_j(\eta,\zeta) = \sum_{k=1}^{4} M^k(\eta,\zeta) T_j^k \tag{17}$$
$$q_j(\eta,\zeta) = \sum_{k=1}^{4} M^k(\eta,\zeta) q_j^k$$

with the bilinear shape functions M^k defined as,

$$\begin{aligned} M^1(\eta,\zeta) &= \frac{1}{36}(3-4\eta)(3-4\zeta) \\ M^2(\eta,\zeta) &= \frac{1}{36}(3+4\eta)(3-4\zeta) \\ M^3(\eta,\zeta) &= \frac{1}{36}(3+4\eta)(3+4\zeta) \\ M^4(\eta,\zeta) &= \frac{1}{36}(3-4\eta)(3+4\zeta) \end{aligned} \tag{18}$$

Introducing the above discretization in the BIE in Eqn. (8), and collocating the discretized BIE at each of the boundary nodes ξ_i there results

$$C(\xi_i)\,T(\xi_i) + \sum_{j=1}^{N}\sum_{k=1}^{NPE} H_{ij}^{k} T_j^{k} = \sum_{j=1}^{N}\sum_{k=1}^{NPE} G_{ij}^{k}\, q_j^{k} \tag{19}$$

where the influence coefficients H_{ij}^{k} and G_{ij}^{k} are defined as

$$H_{ij}^{k} = \oint_{\Delta S_j} q^{*}(x,\xi_i)\, M^{k}(\eta,\zeta)\, dS(x) \tag{20}$$
$$G_{ij}^{k} = \oint_{\Delta S_j} T^{*}(x,\xi_i)\, M^{k}(\eta,\zeta)\, dS(x)$$

These influence coefficients are evaluated numerically via Gauss-Legendre quadratures with special adaption when evaluating the integrals on ΔS_i (for the element upon which the source point ξ_i lies) and heuristic adaptive quadratures for elements that are close to the node of interest (see Appendix). The surface integrals in the above equation depend purely on the local geometry of the element and the location of the source point ξ_i. Upon collocation of the above at every boundary node where the temperature and heat flux are defined, the following algebraic form is obtained:

$$[H]\{T_s\} = [G]\{q_s\} \tag{21}$$

Here the influence matrices $[H]$ and $[G]$ are evaluated numerically using quadratures. Once the boundary conditions are specified, the above is re-arranged in standard $[A]\{x\} = \{b\}$ and the ensuing equations are solved by direct or iterative methods. In a fully conjugate solution using the algorithm described in this paper, these BEM equations are solved subject to the following boundary condition at external and internal bounding walls which are in contact with the fluid and denoted by $\Gamma_{\text{conjugate}}$:

$$T_{\text{s}}|_{\Gamma_{\text{conjugate}}} = T_f \tag{22}$$

In the reduced periodic 3-D computational model to be discussed in the example section, adiabatic conditions are also imposed at the flowfield periodic surfaces in the spanwise direction, i.e. there

$$q_s = 0 \tag{23}$$

Once these equations are solved, the heat flux is known at all surface nodes. This is the sought-after quantity in the CHT algorithm to be shortly outlined. In the case where the conduction problem is solved without further treatment, the basic BEM code had options of using an LU decomposition for small numbers of equations and a GMRES iterative solver with an incomplete LU (ILU) pre-conditioning for large numbers of equations. When the number of equations gets very large, storage becomes an important issue, as the coefficient matrix is fully-populated. We will discuss an effective treatment of such problems in a later section.

3.3 CHT Algorithm

The Navier-Stokes equations for the external fluid flow and the heat conduction equation for heat conduction within the solid are interactively solved to steady state through a time-marching algorithm. The surface temperature obtained from the solution of the Navier-Stokes equations is used as the boundary condition of the boundary element method for the calculation of heat flux through the solid surface. This heat flux is in turn used as a boundary condition for the Navier-Stokes equations in the next time step. This procedure is repeated until a steady-state solution is obtained. In practice, the BEM is solved every few cycles of the FVM to update the boundary conditions, as intermediate solutions are not physical in this scheme. In the calculations carried out in this study, the BEM solution was run every ten cycles of the finite volume solver. This is referred to as the temperature forward/flux back (TFFB) coupling algorithm as outlined below:

• FVM Navier-Stokes solver:

1. Begins with initial adiabatic boundary condition at solid surface.
2. Solves compressible NS for fluid region.
3. Provides temperature distribution to BEM conduction solver after a number of iterations.
4. Receives flux boundary condition from the BEM as input for next set of iterations.

• BEM conduction solver:

1. Receives temperature distribution from FVM solver.
2. Solves steady-state conduction problem.
3. Provides flux distribution to FVM solver.

The transfer of heat flux from the BEM to the FVM solver is accomplished after under-relaxation.

$$q = \beta\, q_{o\,ld}^{BEM} + (1-\beta) q_{new}^{BEM} \tag{24}$$

with β taken as 0.2 in all reported calculations. The choice of the relaxation parameter is through trial and error. In certain cases, it has been our experience that a choice of larger relaxation parameter can lead to non-convergent solutions [50]. The process is continued until the NS solver converges and wall temperatures and heat fluxes converge, that is until Eqn. (6) is satisfied within a set tolerance

$$\begin{aligned} \| \underset{\sim}{T}_{f} - \underset{\sim}{T}_{s} \| < \epsilon_T \\ \| \underset{\sim}{q}_{f} - \underset{\sim}{q}_{s} \| < \epsilon_q \end{aligned} \tag{25}$$

where the tolerances ϵ_T and ϵ_q are taken as 0.001.

It should be noted that alternatively, the flux could be specified as a boundary condition for the BEM code leading to a flux forward temperature back (FFTB) approach. However, when a fully conjugate solution is undertaken, this would amount to specifying second kind boundary

conditions completely around the surface of a domain governed by an elliptic equation, resulting in a non-unique solution. The TFFB algorithm avoids such a situation.

3.4 Interpolation Between BEM and FVM Grids

An issue arises in information transfer between CFD and BEM as there exists a significant difference in the levels of discretization between the two meshes in a typical CHT simulation. Accurate resolution of the boundary layer requires a FVM surface grid which is much too fine to be used directly in the BEM. A much coarser surface grid is typically generated for the BEM solution of the conduction problem. The disparity between the two grids requires a general interpolation of the surface temperature and heat flux between the two solvers as it is not possible in general to isolate a single BEM nodes and identify a set of nearest FVM nodes. Indeed in certain regions where the CFD mesh is very fine, a BEM node can readily be surrounded by tens or more FVM nodes.

A distance-weighted interpolation, reminiscent of radial basis function (RBF) interpolation [23], is adopted for transfer of temperature and flux values between the BEM and CFD grids. Consider Fig. 3(a), here the location of a BEM node is identified on the right-hand-side by a star-like symbol. Let us consider the problem of transferring the temperature from the FVM grid to the BEM grid. Let us denote the position of the BEM node of interest by $\vec{r}_i$, and the location of an FVM node by $\vec{r}_j$. The radial distance from every FVM node to the BEM node of interest is then $r_{ij} = |\vec{r}_j - \vec{r}_i|$. Let us suppose that the number of all FVM surface nodes lying within a ball of radius R_{max} centered

about $\vec{r}$ is N_{ball}. Moreover, let us denote two cases. Case I where all $r_{ij} > \epsilon$ and case II where there is an FVM node located at $\vec{r}_{j,\epsilon}$ such that $r_{ij} \leq \epsilon$, where ϵ is a tolerance. Then, the value of the temperature at the BEM node $\vec{r}_j$ is evaluated as

$$T_{BEM}(\vec{r}_i) = \frac{\sum_{j=1}^{N_{ball}} \frac{T_{CFD}(\vec{r}_i)}{r_{ij}}}{\sum_{j=1}^{N_{ball}} \frac{1}{r_{ij}}} \qquad \text{for case I} \tag{26}$$

$$= T_{CFD}(\vec{r}_{j,\epsilon}) \qquad \text{for case II}$$

In all calculations, the maximum radius R_{max} of the sphere is set to 2.5% of the maximum distance within the solid region and ϵ is set to $\epsilon = R_{max}$ x 10^{-20}. These limits may be adjusted to suit the problems at hand.

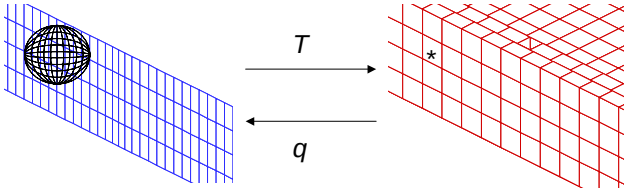

(a) transfer of nodal temperatures and fluxes between CFD and BEM grids.

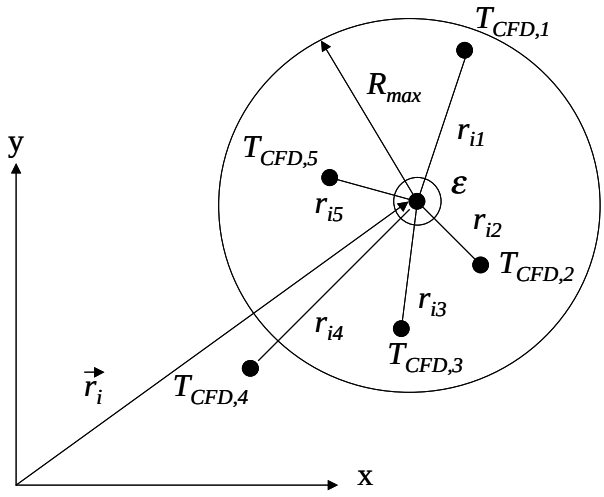

(b) 2-D illustration of five CFD nodes nearest to a BEM node located at $\vec{r}_i$.

Figure 3. Transfer of nodal values from FVM and BEM (and back) independent surface meshes is performed with a distance weighted radial interpolation.

4 Strategy for BEM Models of Large-Scale Three-Dimensional Heat Conduction Problems

As mentioned, the BEM is ideally suited for the solution of linear and non-linear heat conduction problems and is a particularly advantageous numerical method due to its boundary-only feature, however, the coefficient matrix of the resulting system of algebraic equations is fully populated. For large-scale problems that occur in engineering 3-D modeling of complex structures this poses very serious numerical challenges due to large storage requirements and iterative solution of large sets of non-sparse equations. This problem has been approached in the BEM community by one of two approaches: the artificial subsectioning of the 3-D model into a multi-region model in conjunction with block-solvers reminiscent of the FEM frontal solvers [51,52] and the adoption of multipole methods in conjunction with the GMRES non-symmetric iterative solver [53-55]. The first approach of domain decomposition or subsectioning produces a sparse block coefficient matrix that is efficiently stored and has been successfully implemented in commercial codes such as BETTI and GPBEST in the context of continuous boundary elements. However, the method requires generation of complex data-structures identifying connecting regions and interfaces prior to analysis. The second approach is very efficient, however, it requires complete re-write of the BEM code to adopt multipole formulation. Recently, a novel technique using wavelet decomposition has been recently proposed to reduce matrix storage requirements without need for a major alteration of traditional BEM codes [56].

We propose to adopt the first approach, however, we do not use a block solver but rather a region-by-region iterative solver. Although it was reported earlier in the literature that this process sometimes has difficulty converging for nonlinear problems [34,35], it has been shown [36] that when properly implemented, the iterative process converges very efficiently and can offer very substantial savings in memory. Moreover, the technique does not require any complex data-structure preparation. Indeed, the approach is somewhat transparent to the user, a significant advantage in coupling BEM to other field solvers. It should be noted that this sub-sectioning method is under current development and has not yet been integrated into the CHT solver at the

point of writing this paper, and thus the technique along with an example 3-D conduction solution are presented herein with this explicit caveat.

The solution algorithm for the multi-region BEM iteration process consists on the steps described as follows. First, the problem domain Ω is identified along with the corresponding boundary conditions over the boundary Γ. A typical problem definition along with the corresponding boundary conditions and a sample single-region BEM discretization is depicted below.

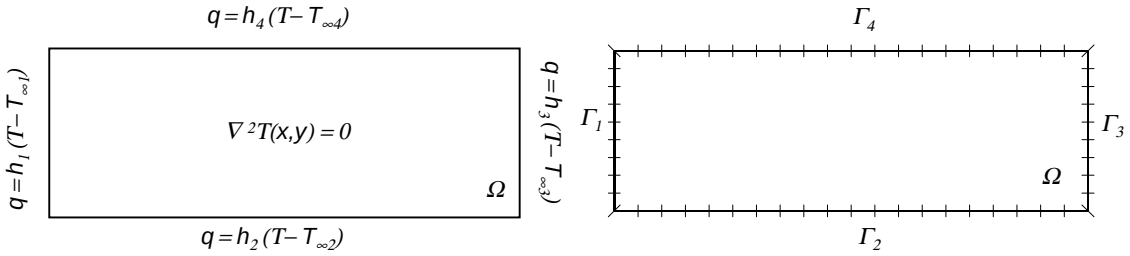

Figure 4. BEM problem domain, boundary conditions, and single region discretization.

If a standard BEM solution process were to be adopted a system of influence coefficient matrices and boundary values of size N, where N is the number of boundary nodes used to discretize the problem, will be formed. The number of floating point operations required to arrive at the algebraic system is proportional to N^2 as well as direct memory allocation also proportional to N^2. With the aid of the boundary condition distribution, the system is re-arranged as

$$[H]\{T\} = [G]\{q\} \Rightarrow [A]\{x\} = \{b\} \tag{27}$$

where $\{x\}$ represents the unknowns $\{T\}$ or $\{q\}$ around the boundary nodal distribution. The solution to the algebraic system for the boundary unknowns can be performed using a direct solution method such as LU decomposition requiring floating point operations proportional to N^3 or an indirect method such as Bi-conjugate Gradient or General Minimization of Residuals which, in general, require floating point operations proportional to N^2 to achieve convergence.

If a multi-region BEM iteration solution process were to be adopted instead, the domain is divided into K subdomains and each one is independently discretized. It is worth mentioning that the BEM discretizations of neighboring subdomains does not have to be coincident, this is, at the connecting interface, boundary elements and nodes from the two colliding subdomains are not required to be structured following a sequence or particular position, the only requirement at the connecting interface is that it forms a closed boundary with the same path on both sides. Later, it will be shown that the information between neighboring subdomains separated by an interface will be passed through an interpolation process as opposed than just a node to node connection.

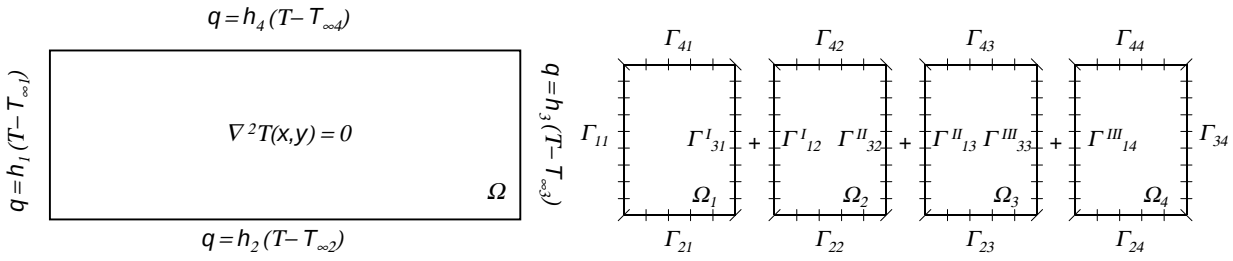

Figure 5. BEM problem domain, boundary conditions, and single region discretization.

Figure 5 above shows the same problem depicted in Fig. 4 with a multi-region BEM discretization of four ($K = 4$) subdomains. The boundary value problem will now be solved independently over each subdomain where initially, a guessed boundary condition is imposed over the interfaces in order to ensure the well-posedness of each subproblem. For instance, the boundary value problem of subdomain Ω_1 is transformed into the algebraic analogue of corresponding influence coefficient matrices and nodal boundary values as

$$\nabla^2 T_{\Omega_1}(x, y) = 0 \Rightarrow [H_{\Omega_1}]\{T_{\Omega_1}\} = [G_{\Omega_1}]\{q_{\Omega_1}\} \tag{28}$$

The composition of this algebraic system requires floating point operations proportional to the square of the number boundary nodes in the subdomain (n^2)as well as for direct memory

allocation (n^2). This new proportionality number n is roughly equivalent to

$$n \approx \frac{2N}{K+1} \tag{29}$$

as long as the discretization along the interfaces has the same level of resolution as the discretization along the boundaries. Direct memory allocation requirement for later algebraic manipulation is now reduced to a proportion of n^2 as the influence coefficient matrices can easily be stored in ROM memory for later use after the boundary value problems on remaining subdomains have been effectively solved. For the example shown here where the number of subdomains is $K = 4$ the new proportionality value n is approximately equal to $n \approx 2N/5$. This simple multi-region example reduces the memory requirements to about $n^2/N^2 = (4/25) = 16\%$ of the standard BEM approach.

The algebraic system for subdomain Ω_1 is rearranged, with the aid of given and guessed boundary conditions, as

$$[H_{\Omega_1}]\{T_{\Omega_1}\} = [G_{\Omega_1}]\{q_{\Omega_1}\} \;\Rightarrow\; [A_{\Omega_1}]\{x_{\Omega_1}\} = \{b_{\Omega_1}\} \tag{30}$$

The solution of the new algebraic system of subdomain Ω_1 requires now a number of floating point operations proportional to $n^3/N^3 = (8/125) = 6.4\%$ of the standard BEM approach if a direct algebraic solution method is employed, or a number of floating point operations proportional to $n^2/N^2 = (4/25) = 16\%$ of the standard BEM approach if an indirect algebraic solution method is employed. For both, floating point operation count and direct memory requirement the reduction is dramatic. However, as the first set of solutions for the subdomains were obtained using guessed boundary conditions along the interfaces, the global solution needs to follow an iteration process and convergence criteria.

Globally, the floating point count for the formation of the algebraic setup for all K subdomains must be multiplied by K, therefore, the total operation count for the coefficient matrices computation is given by,

$$K\frac{n^2}{N^2} \approx \frac{4K}{(K+1)^2} \tag{31}$$

or, for this particular case with $K = 4$, $Kn^2/N^2 = 16/25 = 64\%$ of the standard BEM approach. Moreover, the more significant reduction is revealed in the RAM memory requirements as only the memory needs for one of the subdomains must be allocated at a time. The rest of the coefficient matrices for the remaining subdomains are temporarily stored in ROM memory until access and manipulation is required. Therefore, for this case of $K = 4$, the true memory reduction is $n^2/N^2 = 4/25 = 16\%$ of the standard BEM approach.

With respect to the algebraic solution of the system of Eqn. (30), if a direct approach as the LU decomposition method is employed for all subdomains, the LU factors of the coefficient matrices for all subdomains can be computed only once at the first iteration step and stored in ROM memory for later use during the iteration process for which only a forward and a backward substitution will be required to solve the system at hand. This feature allows a significant reduction in the operational count through the iteration process until convergence is achieved, as only a number of floating point operations proportional to n as opposed to n^3 is required at each iteration step. To this computation time is added the access to ROM memory at each iteration step which is usually larger than the access to RAM. Moreover, when applied to the CHT problem, again storage of the LU factors offers significant computational savings over using an iterative method. However, use of direct solvers requires each sub-section to be kept at a discretization close to 1,000 bi-linear boundary elements.

The iteration process follows the initial step of guessing the interface conditions. This is a crucial step as the more physical information the initial guess incorporates the less iterations will be required to reduce the error. The simplest choice is to assume adiabatic conditions at the artificial interfaces. Results from several numerical studies show this approach leads to intial temperature fields that are far from the final temperature field and which are slow to update iteratively. A rather more efficient initial guess can be made using a physically based 1-D heat

conduction argument for every node on the external surface to every node at the interface. The following algebraic initial guess for any interfacial node can be readily derived, see [57] for details, as

$$T_i = \frac{\sum_{j=1}^{N_T} B_{ij} T_j - \sum_{j=1}^{N_q} B_{ij} R_{ij} q_j + \sum_{j=1}^{N_h} \frac{B_{ij} H_{ij} T_{\infty j}}{H_{ij}+1}}{S_i - \sum_{j=1}^{N_T} B_{ij} + \sum_{j=1}^{N_h} \frac{B_{ij} H_{ij}}{H_{ij}+1}} \tag{32}$$

where N_T, N_q, and N_h are the number of first, second, and third kind boundary conditions specified at the external (non-interfacial) surfaces and

$$\begin{aligned} B_{ij} &= \frac{A_j}{|r_{ij}|} \\ R_{ij} &= \frac{\vec{r_{ij}} \cdot \widehat{n_j}}{k} \\ H_{ij} &= \frac{h_j}{k}(\vec{r_{ij}} \cdot \widehat{n_j}) \\ S_i &= \sum_{j=1}^{N} \frac{A_j}{|r_{ij}|} \end{aligned} \tag{33}$$

with $N = N_T + N_q + N_h$, the thermal conductivity of the medium is k, the film coefficient at the j-th convective surface is h_j, the outward-drawn normal to any surface is $\widehat{n_j}$, the position vector from the interfacial node i to the external surface node j is $\vec{r_{ij}}$ and its magnitude is $r_{ij} = |\vec{r_{ij}}|$, while the area of element j denote by A_j is readily computed as

$$A_j = \oint_{\Gamma_j} d\Gamma(x,y,z) = \int_{-1}^{+1}\int_{-1}^{+1} J_j(\eta,\zeta) d\eta d\zeta \tag{34}$$

Once the initial temperatures are imposed as boundary conditions at the interfaces, a resulting set of normal heat fluxes along the interfaces will computed. These are then non-symmetically averaged in an effort to match the heat flux from neighboring subdomains. Considering a two-domain substructure the averaging at the interface is explicitly given as,

$$q^I_{\Omega_1} = q^I_{\Omega_1} - \frac{q^I_{\Omega_1} + q^I_{\Omega_2}}{2} \tag{35}$$

and,

$$q^I_{\Omega_2} = q^I_{\Omega_2} - \frac{q^I_{\Omega_2} + q^I_{\Omega_1}}{2} \tag{36}$$

to ensure the flux continuity condition $q^I_{\Omega_1} = -q^I_{\Omega_2}$ after averaging. Compactly supported radial basis interpolation can be employed for the flux average to account for unstructured grids along the interface from neighboring subdomains.

Using these fluxes the BEM equations are again solved leading to mismatched temperatures along the interfaces for neighboring subdomains. These temperatures are interpolated, if necessary, from one side of the interface to the other side using a compactly supported radial basis functions to account for the possibility of interface mismatch between the adjoining substructure grids. Once this is accomplished, the temperature is averaged out at each interface. Illustrating this for a 2 domain substructure, again we have for regions 1 interface,

$$T^I_{\Omega_1} = \frac{T^I_{\Omega_1} + T^I_{\Omega_2}}{2} \tag{37}$$

and region 2 interface

$$T^I_{\Omega_2} = \frac{T^I_{\Omega_1} + T^I_{\Omega_2}}{2} \tag{38}$$

In case a real or physical interface exists and a thermal contact resistance is present between the connecting subdomains, the temperatures are averaged out as,

$$T^I_{\Omega_1} = \frac{T^I_{\Omega_1} + T^I_{\Omega_2}}{2} + R^{''} q^I_{\Omega_1} \tag{39}$$

and,

$$T^I_{\Omega_2} = \frac{T^I_{\Omega_1} + T^I_{\Omega_2}}{2} + R^{''} q^I_{\Omega_2} \tag{40}$$

where $R^{''}$ is the value of the thermal contact resistance imposing a jump on the interface temperature values. These now matched temperatures along the interfaces are used as the next set of boundary conditions.

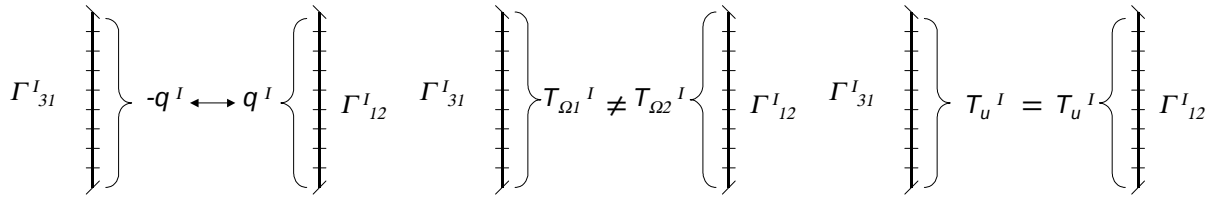

(a) (b) (c)

Figure 6. Iteration along the interface (a) imposed heat flux, (b) mismatched resulting temperatures, and (c) interpolated and averaged out temperatures as new boundary conditions.

Finally, in order to provide an improved initial guess to the BEM solver, a two-level discreetization approach is employed. The initial guess provided by physically-based procedure in Eq. (32) is used to solve the conduction solution for a constant element conduction model. This coarse computation is carried out using the same discretization as the bi-linear model, however, all nodes are collapsed to a single central node, and this requres 1/64th of the work required to solve the bi-linear model. Upon convergence of the constant element model, a full bi-linear solution is subsequnetly computed with the constant element model providing the initial guess.

This iteration process is continued until a convergence criterion is satisfied. A measure of convergence may be defined as the L_2 norm of mismatched temperatures along all interfaces as:

$$L_2 = \sqrt{\frac{1}{K \cdot N^I} \sum_{k=1}^{K} \sum_{i=1}^{N^I} (T^I - T_u^I)^2} \tag{41}$$

This norm measures the standard deviation of BEM computed interface temperatures T^I and averaged-out updated interface temperatures T_u^I. The iteration routine can be stopped once this standard deviation reaches a small fraction ϵ of ΔT, where ΔT is the maximum temperature span of the global field. This concludes the numerical developments in this paper, attention is now given to numerical examples.

5 Numerical Results and Discussion

We now present results of a full conjugate solution of a film-cooled blade under operating conditions which match a planned experiment at NASA Glenn Research center and assumes periodicity in the spanwise direction for one pitch of film-cooling hole patterns. We compare results of this simulation to those obtained from the standard two temperature method. This simulation uses the standard BEM approach to heat conduction. We also present results from several simulations fo the sub-sectioning BEM approach to heat conduction modeling in 2-D and in 3-D. In 3-D, a square cross-section bar, a thrust vector control vane, and a cooled turbine vane geometry are used to illustrate the sub-sectioning method described in this report.

5.1 CHT simulation of a 3-D Film-cooled Turbine Blade

Film cooling is commonly used in turbine designs to produce a buffer layer of relatively cool air between the turbine blade and the hot freestream gas in the first and second rows of blades and vanes. The CHT computation is carried out on a computational model of a realistic film-cooled turbine vane accounting for the three-dimensional vane geometry including plena and film holes and is based on a Honeywell film-cooled engine design, see Heidmann et al. [2]. The geometry of this test vane is based on the engine vane midspan coordinates, and is scaled up by a factor of 2.943 to allow matching of engine exit Mach number (0.876) and exit Reynolds number ($2.9 \text{ x } 10^6$ based on true chord) with atmospheric inlet conditions. The test vane has a true chord of $0.206\,m$. Since the test vane is of constant cross section, only one spanwise pitch of the film hole pattern was discretized, with periodicity of the flow-field enforced at each end. This simplification assumes no effect of endwalls, but greatly reduces the number of grid points required to model the vane. However, the thermal boundary conditions enforced at these ends in the conduction analysis were adiabatic. The vane has two plena which feed 12 rows of film cooling holes as well as trailing-edge ejection slots, see Fig. 7. Trailing edge ejection is blocked in the computation as the planned experiment has no slot cooling. Detailed geometrical data for each row of film holes as well as hole distribution are provided in [2]. A multi-block grid approach is adopted to model this complex geometry and generated the FVM grid using the

topology-based algebraic grid-generation program GridPro^{TM} [17] with the final grid consisting of 140 blocks and a total of 1.2×10^6 finite volume computational cells. The FVM grid consists of 20 cells across both the inlet and outlet boundaries, 60 cells on the periodic boundary, over 200 cells around the vane, and 44 cells from the vane to the periodic boundary.

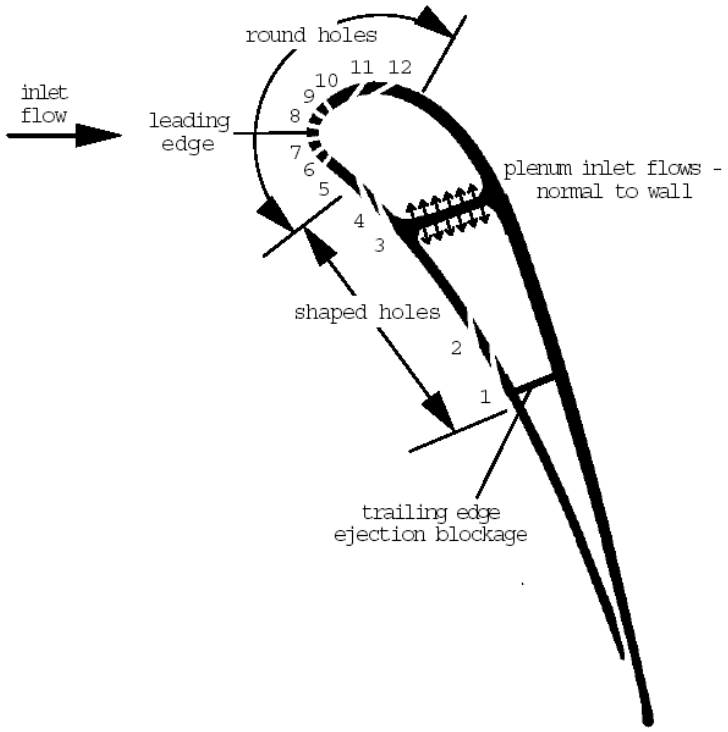

Figure 7. Film-cooled blade profile used in the CHT simulation.

A blade-to-blade view of the FVM grid is shown in Fig. 8 and Fig. 9 shows the FVM grid in the leading edge region of the vane.

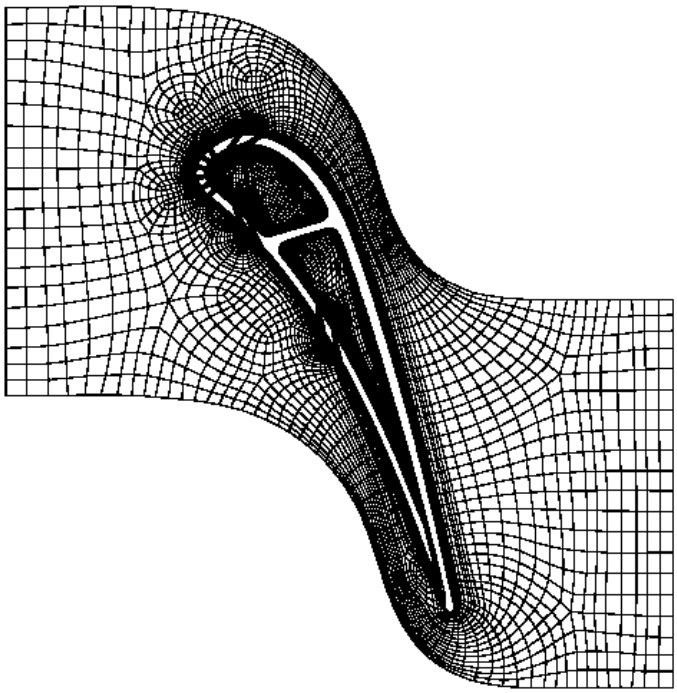

Figure 8. Blade to blade computational grid cross section.

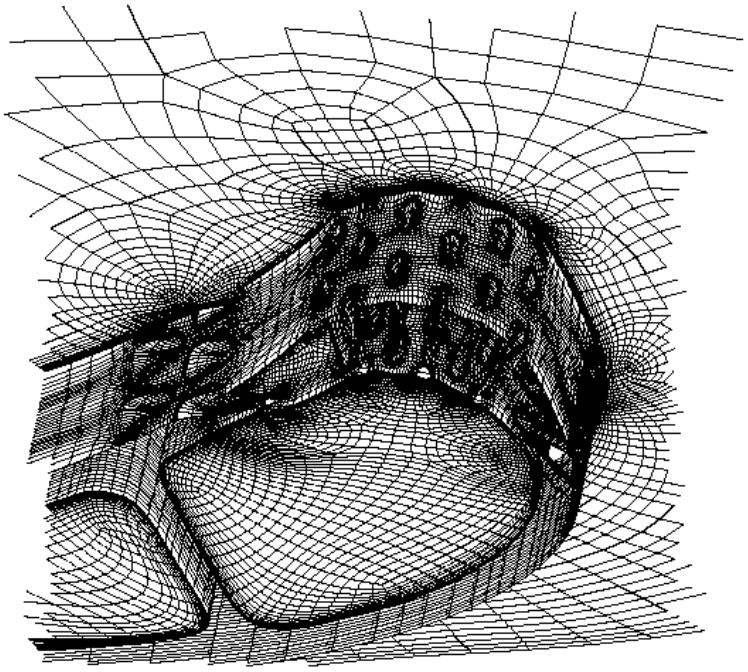

Figure 9. FVM grid in the leading edge region of the blade.

The flow conditions for all simulations use a free-stream inlet flow to the vane at an angle of $0°$ to the axial direction, with all temperatures and pressures normalized by the inlet stagnation values of $3109R$ and 10 atmospheres, respectively. The inlet turbulence intensity is set at 8.0% and the turbulence scale is 15.0% of vane true chord. Other inflow quantities are set by means of the upstream-running Riemann invariant. The vane downstream exit flow is defined by imposing a constant normalized static pressure of 0.576, which was empirically determined to yield a desired exit Mach number of 0.876. Periodicity was enforced in both the blade-to-blade and spanwise directions based on vane and film hole pitches, respectively. Moreover, in order to maintain a true periodic solution, inflow to the plena was provided by defining a region of each plenum wall as an inlet and introducing uniform flow normal to the wall. In Fig. 8, these regions are shown to lie on either side of the internal wall that separates the two plena. In practice, there will be spanwise flow in the plenum, but bleed of the plenum flow into the film holes results in a spanwise-varying mass flow rate and static pressure, which would violate spanwise periodicity imposed in this particular reduced computational model. The non-dimensionalized inflow stagnation temperature to the plena was 0.5, corresponding to a coolant temperature of $1554.5R$. the velocity was fixed to the constant value required to provide the design mass flow rate to each plenum, and static pressure was extrapolated from the interior. The inflow patch for each plenum was defined to be sufficiently large to yield very low inlet velocities (Mach number < 0.05), allowing each plenum to approximate an ideal plenum. All solid walls were imposed with a no-slip boundary condition. The blade metal material is taken as Inconel with a conductivity of $k_{blade} = 1.34\ Btu/hr\,in\,R$ taken at $2174.9R$ which is estimated to be the average blade temperature.

The FVM metal surface grid consists of $38,000$ cells at the 4th level of multi-grid. The grid was coarsened to generate a BEM grid of $1,3000$ bilinear cells with $5,2000$ nodal unknowns. Two cases are computed in the numerical simulation in order to obtain the metal temperature:

1. The traditional two-temperature approach, whereby two different isothermal wall boundary condition extended to all wall surfaces, including the film hole surfaces and plenum surfaces. Two solutions were generated with constant wall temperatures T_w of $T_{w,1} = 2174.9R$ and $T_{w,2} = 2485.6R$ imposed on all blade surfaces. The flowfield was computed from the plena through the cooling holes and over the blade. The predicted wall heat fluxes at each node q''_w computed from each of these isothermal solutions were used to solve simultaneously for adiabatic wall temperature, T_{aw}, and heat transfer coefficient, h, referenced to the computed adiabatic wall temperature, under the assumption that T_{aw} and h are independent of the wall temperature. That is at each node we have

$$\begin{aligned} q''_w &= h(T_{w,1} - T_{aw}) \\ q''_w &= h(T_{w,2} - T_{aw}) \end{aligned} \tag{42}$$

In turn, these film coefficient and associated adiabatic wall distributions were used in the BEM to compute metal temperatures.

2. A full CHT solution was carried out using the same grids and boundary conditions above except at the blade surface where conjugate conditions were imposed. The conjugate solutions converged in 1000 iterations with a BEM conduction calculation performed each 10 FVM iterations. The BEM code was written as a subroutine to the Glenn-HT code and subroutines were coded to exchange information between the two codes in terms of the FVM and BEM grids as well as boundary condition information. The Glenn-HT code was modified to allow for non-isothermal boundary condition specification.

All computations were performed at NASA Glenn Research Center on an SGI Origin 2000 cluster with 32 processors. Flow computations were carried out and considered converged when residuals were driven below 10^{-5}. Results of the blade surface temperatures predicted by the simulations are shown in Fig. 10 for the CHT solution and in Fig. 11 for the two constant

temperature approach. The two temperature distributions are markedly different with a temperature span of $\Delta T = 1720 - 2420R$ across the surface of the blade while the CHT solution predicted a temperature span of $\Delta T = 1620 - 2620R$ across the blade. In addition to CHT computations predicting lower minimum ($100R$ colder) and higher maximum temperatures ($200R$ hotter), the distribution of cold and hot regions are quite different as is evident from the surface plots. For instance, with conduction taken into consideration in the CHT simulation, the thin trailing regions are seen to reach higher temperatures than predicted by the isothermal approach, while the forward plenum region is seen to be effectively cooler. This has severe implications in materials design and subsequent thermal stress analysis of the blade carried out using these metal temperatures.

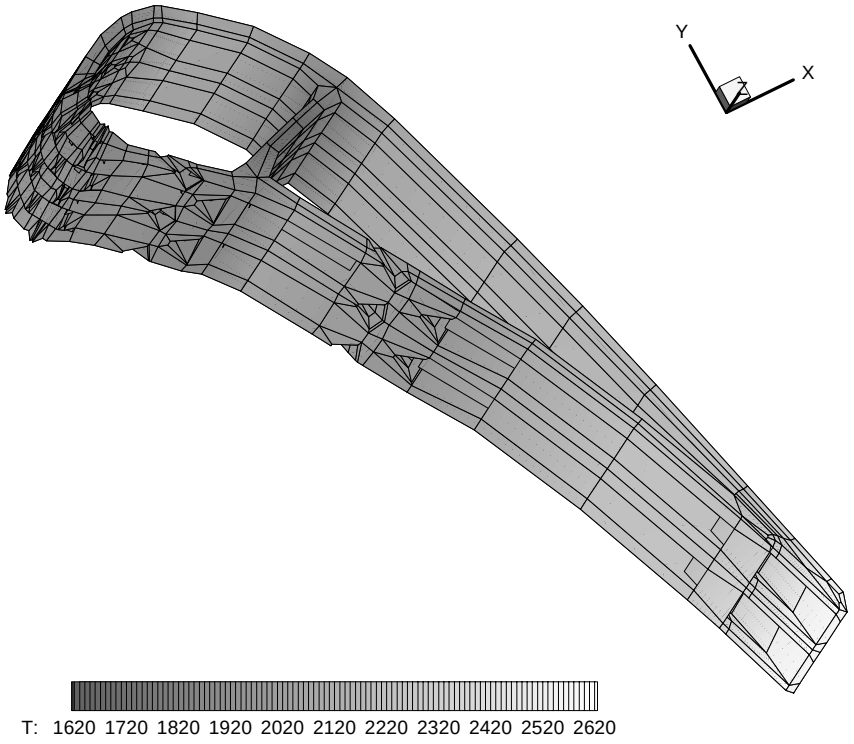

Figure 10. Blade surface temperature predicted by the CHT solution.

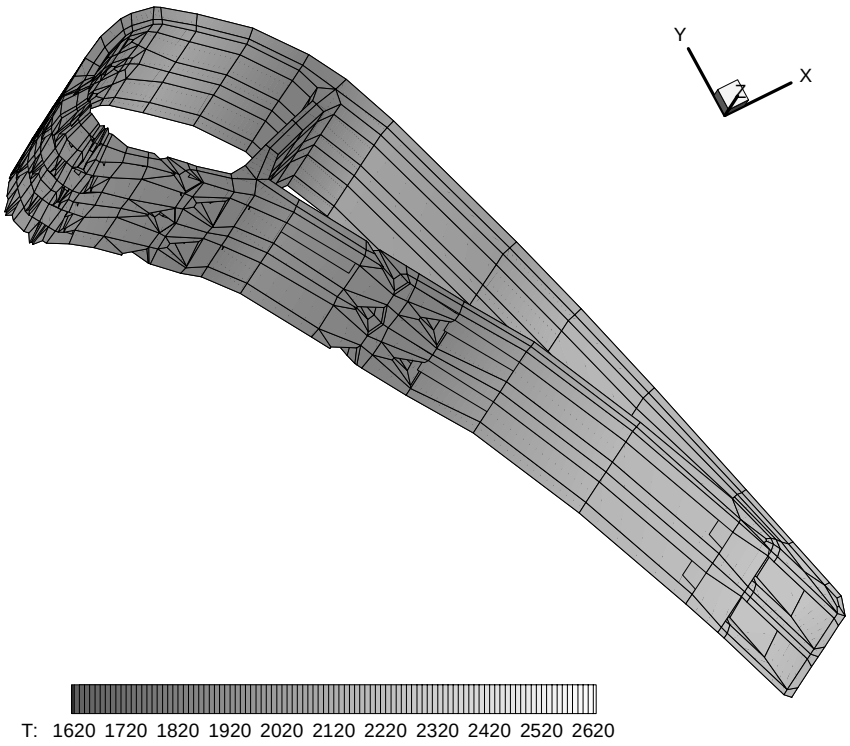

Figure 11. Blade surface temperature predicted by the BEM using h and T_{aw} provided from the two temperature approach.

5.2. Steady Conduction BEM Modeling Using Sub-Sectioning and Iteration

Results are now presented for several simulations using the sub-sectioning iterative method for a pure heat conduction problem. In the first examples the initial guess is carried out using adiabatic conditions at the interface while in the final examples the physically-based reasoning is used to initiate the iteration. The parameter ϵ is set to 10^{-3}. All computations were performed on a Pentium 4, 1.8 GHz PC with 512 MB 800MHz RDRAM.

5.2.1 Steady Conduction Model of a 10-Region 2D Slab

A 2D rectangular slab of dimension 10x1 is initially discretized in a single-region using 440 equally spaced quadratic isoparametric discontinuous boundary elements with a total of 1320 nodes around the boundary. Figure 12 shows the boundary conditions and the BEM discretization

for this problem. The isotherm distribution is plotted in Figure 13. The thermal conductivity was imposed as $k = 1$ W/mK.

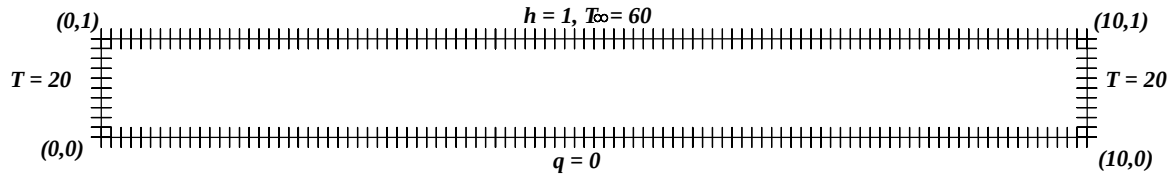

Figure 12. Boundary conditions and BEM discretization of single-region 2D rectangular slab.

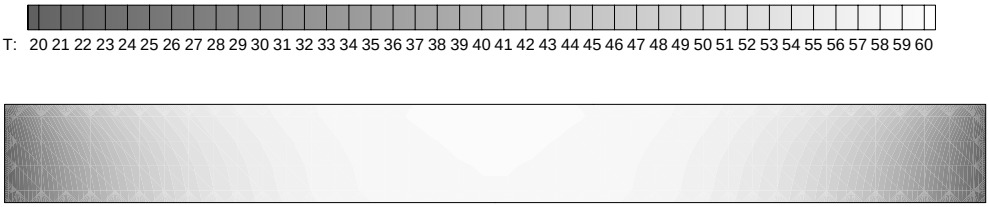

Figure 13. Isotherm distribution for single-region 2D rectangular slab.

Next, the rectangular slab is divided into 10 sub-domains and discretized with 80 quadratic isoparametric discontinuous boundary elements with 240 nodes. Figure 14 shows the boundary conditions and the BEM discretization for this problem. The isotherm distribution is plotted in Figure 15 for the converged solution after 12 iterations with adiabatic conditions used as initial guess at the subsection interface nodes.

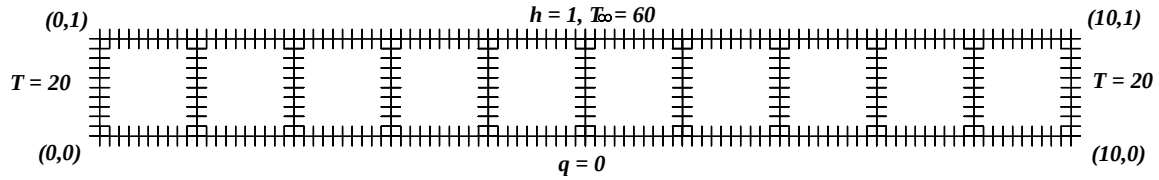

Figure 14. Boundary conditions and BEM discretization of 10-region 2D rectangular slab.

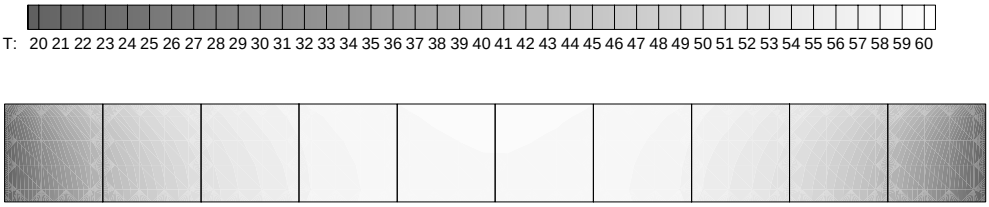

Figure 15. Isotherm distribution for 10-region 2D rectangular slab.

The plot of the L_2 norm progression is shown in Figure 16 for the first 20 iterations, however, the level of convergence of $\epsilon \cdot \Delta T$ was achieved after 12 iterations. Table 1 shows the memory requirement proportions for each case and the computation time for the algebraic setup and solution after the 12 iterations for which $L_2 = 0.04$.

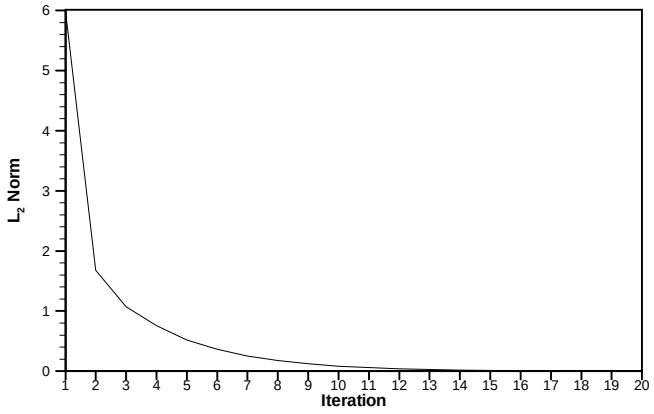

Figure 16. L_2 norm progression for 10-region 2D rectangular slab.

Table 1. Memory and time comparison for 2D rectangular slab problem.

	1-Region	10-Region
Iterations	0	12
L_2 Norm	0	0.04
Memory	100%	3.3%
Time for Setup	50s	16s
Time for Solution	64s	50s

5.2.2 Steady Conduction model of a 5-Region 3D Rectangular Bar

A 3D 5x1 rectangular bar is initially discretized in a single-region using 550 equally spaced bilinear isoparametric discontinuous boundary elements with a total of 2200 nodes around the boundary. Figure 17.a. shows the BEM discretization for this problem along with the isotherm distribution in Figure 17.b. The boundary conditions are distributed as first kind on both end faces with a temperature $T = 0°C$, adiabatic on the bottom face, and convective on the remaining three surfaces with $T_\infty = 100°C$ and $h = 1\,W/m^2K$. The thermal conductivity was imposed as $k = 1\,W/mK$.

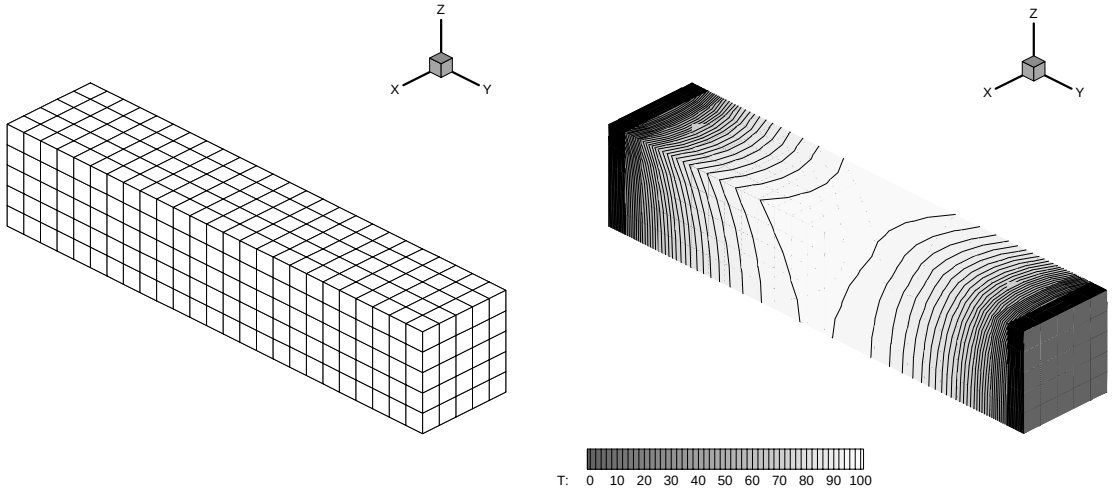

(a) (b)

Figure 17. Rectangular bar example: (a) single region BEM discretization and (b) Isotherm distribution of single-region 3D rectangular slab.

Next, the 3D slab is divided into 5 sub-domains and discretized with 150 bilinear isoparametric discontinuous boundary elements with 600 nodes. Figure 18.a. shows the BEM discretization for this problem and the isotherm distribution is plotted in Figure 18.b. for the converged solution after 4 iterations. Adiabatic conditions are used as an initial guess at the sub-section interface nodes.

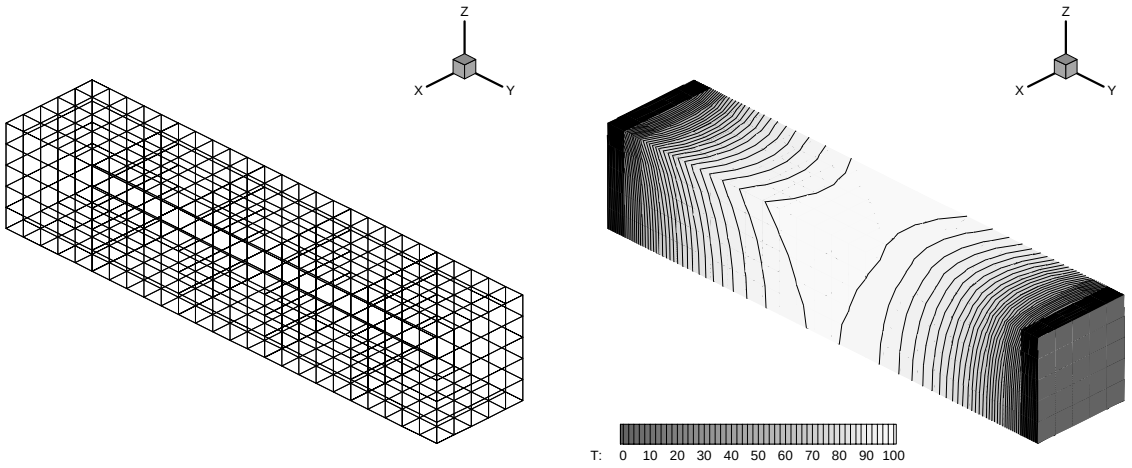

(a) (b)

Figure 18. Five sub-section Model for a rectangular bar: (a) BEM discretization and (b) isotherm distribution of 5-subsection 3D rectangular slab.

The plot of the L_2 norm progression is shown in Figure 19 for the first 10 iterations, however, the level of convergence of $\epsilon \cdot \Delta T$ was achieved after only 4 iterations. Table 2 reveals the memory requirement proportions for each case and the computation time for the algebraic setup and solution after the 4 iterations for which $L_2 = 0.012$.

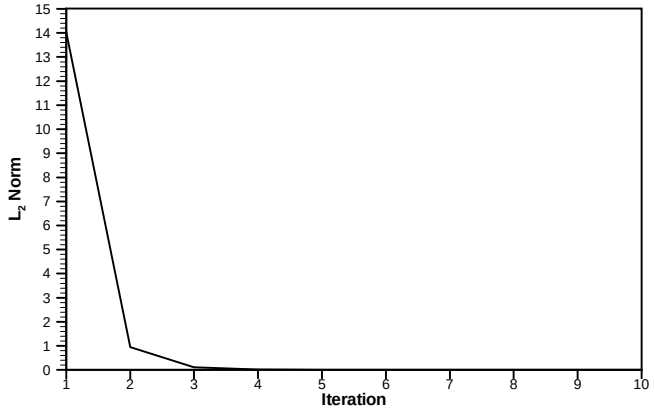

Figure 19. L_2 norm progression for the 5-region 3D slab.

Table 2. Memory and time comparison for 3D slab problem.

	1-Region	5-Region
Iterations	0	4
L_2 Norm	0	0.012
Memory	100%	7.4%
Time for Setup	488s	16s
Time for Solution	374s	86s

5.2.3 Steady Conduction Model of a 3-Region 3D Thrust Vector-Control Vane

A 3D Thrust Vector-Control Vane is initially discretized in a single-region using 610 equally spaced bilinear isoparametric discontinuous boundary elements with a total of 2440 nodes around the boundary. Figure 12.a. shows the BEM discretization for this problem along with the isotherm distribution in Figure 12.b. The boundary conditions were distributed as insulated on the bottom surface, convective on the back surface with $T_\infty = 200$ and $h = 100$, and convective with $T_\infty = 4000°C$ and $h(x) = 1000(x/x_{max})^2 \ \ W/m^2K$ for a maximum of $h = 1000\ W/m^2K$ on the leading edge. A thermal conductivity of $k = 14.9\ W/mK$ was used.

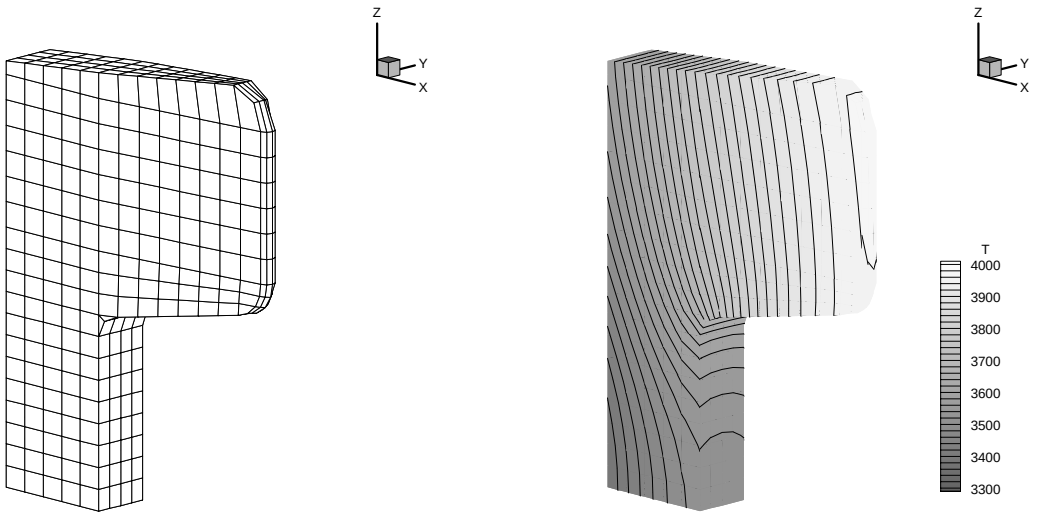

(a) (b)

Figure 20. (a) BEM discretization and (b) Isotherm distribution of single-region 3D Vane.

Next, the 3D Thrust Vector-Control Vane is divided into 3 sub-domains and discretized with a maximum of 300 bilinear isoparametric discontinuous boundary elements with 1200 nodes. Figure 13.a. shows the BEM discretization for this problem and the isotherm distribution is plotted in Figure 13.b. for the non-converged solution after 1 iteration. Figure 14.a shows the non-converged solution isotherms after 40 iterations and finally Figure 14.b. shows the converged solution isotherms after 80 iterations.

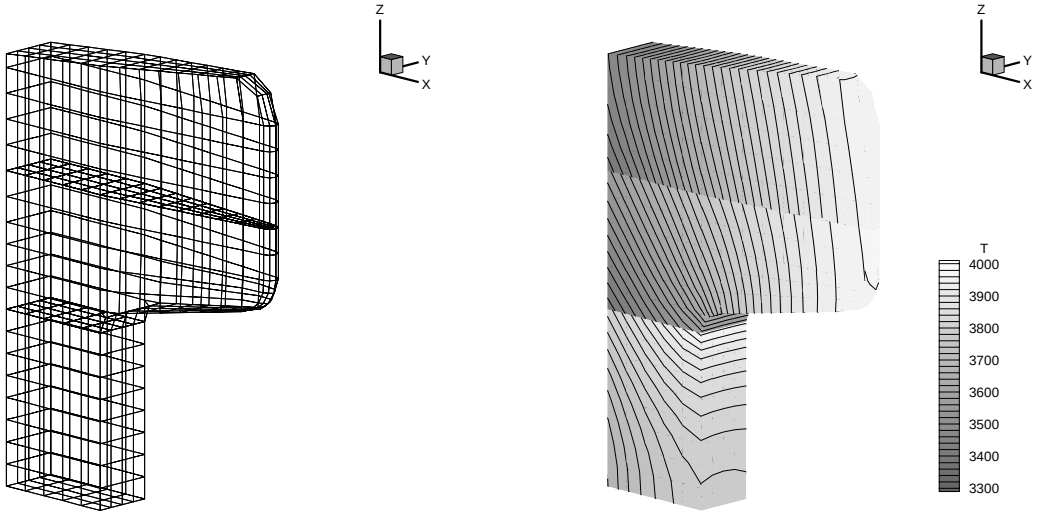

(a) (b)

Figure 21. (a) BEM discretization and (b) Isotherm distribution of 3-region 3D vane after 1 iteration.

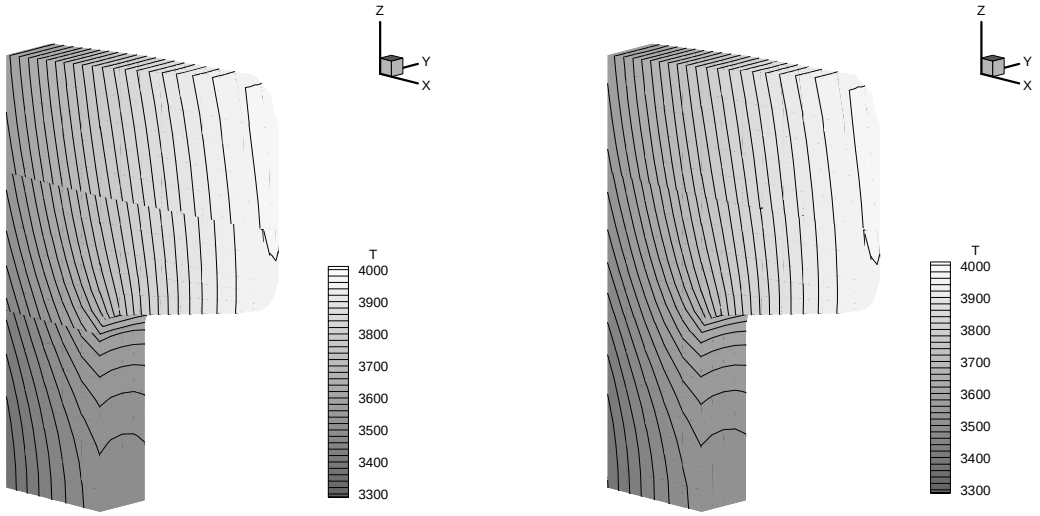

(a) (b)

Figure 22. Isotherm distribution of 3-region 3D vane after (a) 43 iterations and (b) 81 iteration.

The plot of the L_2 norm progression is shown in Figure 23 comparing the iterations for the cases of adiabatic initial guess at the subsection interfacial nodes and physically-based initial guess. When an adiabatic intial guess is made at the sub-structure intefaces, it took 81 iterations to reach the level of convergence of $\epsilon \cdot \Delta T$, while the physically-based intial guess provided an intial error norm of 0.045 (vs 0.32 with the adiabatic guess) which lead to less than 45 iterations to achieve convergence. This clearly demonstrates the effectiveness of the proposed physically-based intial guess in reducing the computational load of the iterative process in this case. Table 3 reveals the memory requirement proportions for each case and the computation time for the algebraic setup and solution. Although final time to solution is comparable, the larger problems could not be tackled by the 1 region approach due to memory requirements and round-off error.

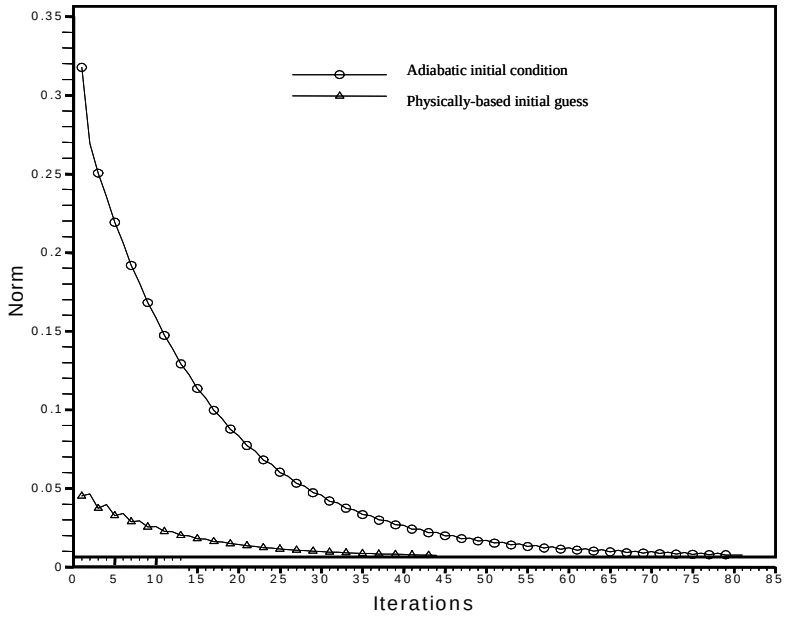

Figure 23. L_2 norm progression for the 3-region 3D vane comparing the iteration for the cases of adiabatic initial guess at the subsection interfacial nodes and physically-based initial guess .

Table 3. Memory and time comparison for 3D slab problem. For the 3-region: (a) adiabatic guess and LU factors computed at each iteration, (b) adiabatic guess and LU factors computed once and stored, (c) Eq. (32) intial guess and LU factors computed once and stored.

	1-Region	3-Region (a)	3-Region(b)	3-Region(c)
Iterations	0	81	81	43
Memory	100%	24%	24%	24%
Time for Setup	605s	391s	1,080s	1,080s
Time for Solution	916s	15,324s	793s	421s

5.2.4 Modeling a 3-D Cooled Blade

Here, a blade with a $10\,cm$ chord and it is 14cm in the spanwise direction. The blade is cooled by two plena, see Fig. 24. The blade is discretized using GridPro^{TM} [17] into 6 subsections with a surface grid of a total of nearly $6,000$ bilinear elements or nearly $24,000$ degrees of freedom, see Fig. 25. Each block is kept at a discretization level near to 1000 bilinear boundary elements. Adiabatic conditions are imposed on the top and bottom surfaces of the blade. Convective boundary conditions are imposed on all other surfaces. The film coefficient on the outer surface of the blade is taken as $h = 1000\,W/m^2K$ with the reference temperature taken as $1000K$, while the cooling plena are both imposed with film coefficients $h = 500$ W/m^2K with the reference temperature taken as linearly varying from $300K$ to $400K$ in the increasing z-direction of the cooling plenum closest to the leading edge, while linearly varying from $500K$ to 400K in the decreasing z-direction of the cooling plenum closest to the trailing edge.

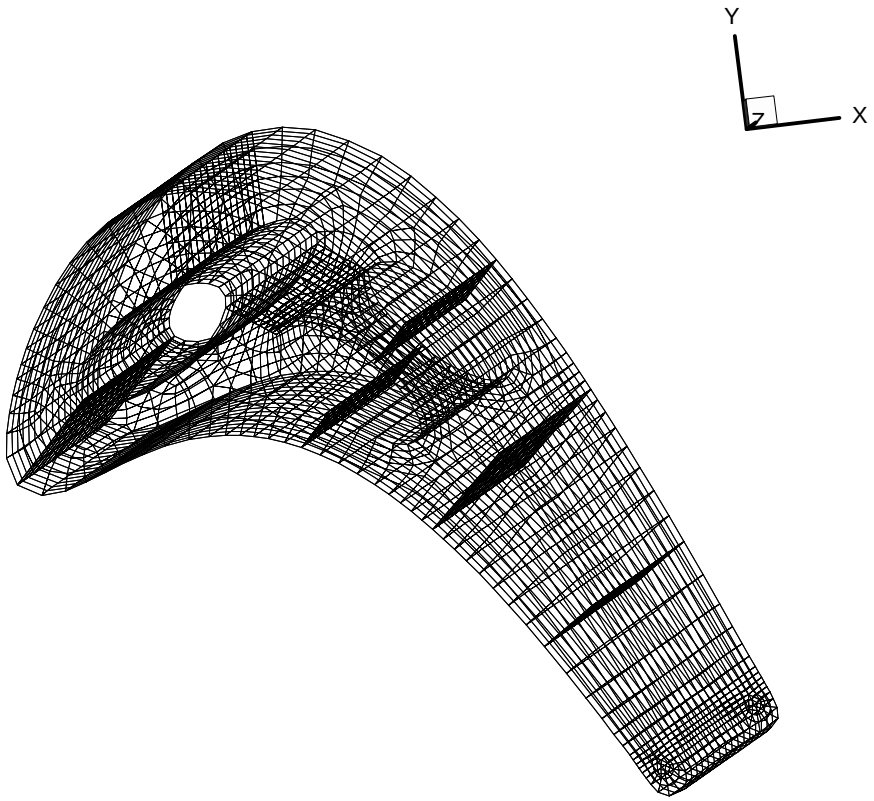

Figure 24. BEM grid for 3D cooled blade.

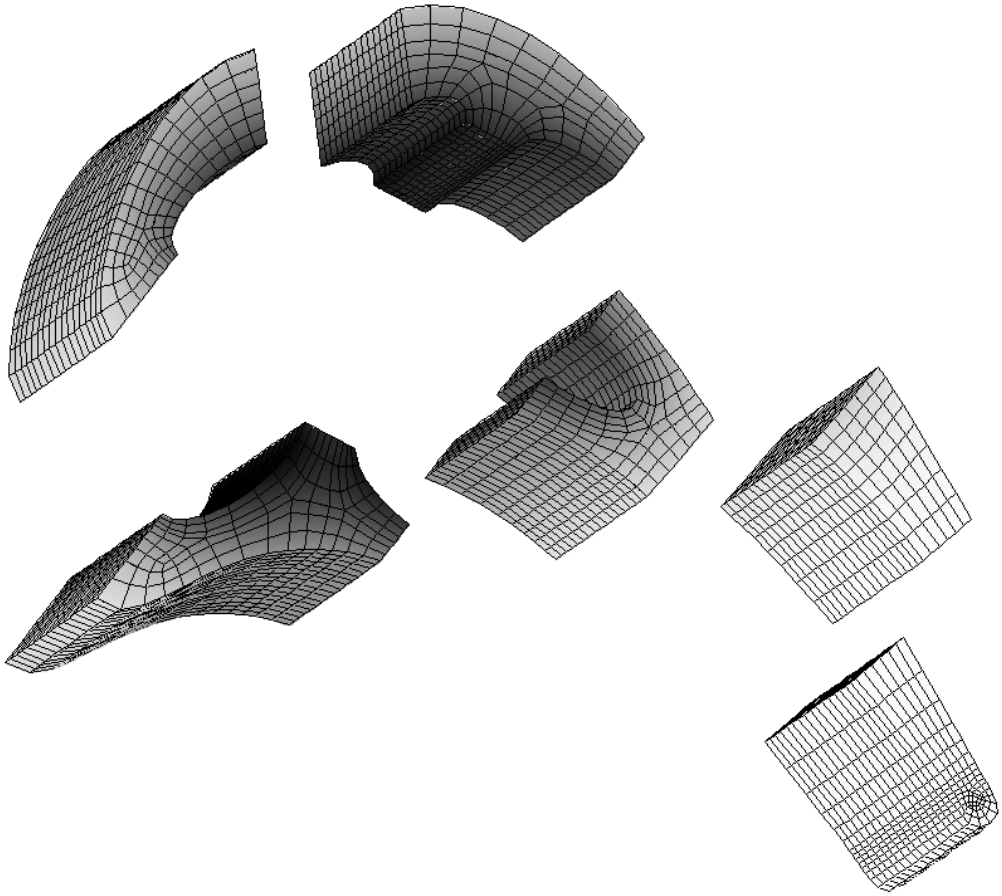

Figure 25. Substructuring of a 3-D plenum-cooled turbine blade.

The physically-based initial guess at the sub-section interfaces using Eqn. (32) provided an excellent starting point for the iteration which converged in 16 steps to provide an L_2 iterative norm, defined in Eqn. (41), of $L_2 = 0.00011698$. It took $34{,}905s$ to set up the matrices, obtain and store their LU factors, and $813s$ to solve the problem iteratively. In this case, the LU factors were stored for each sub-section BEM model, and each iteration consisted of a forward and backward substitution. The resulting temperature plots illustrated in Fig. 25 and Fig. 26 reveal a very smooth distribution across all blocks. The resulting surface heat fluxes are presented in Fig. 27 revealing a very smooth distribution from a minimum of $-180,000\,W/m^2K$ to a maximum of $230,000\,W/m^2K$. It should be noted that the subsectioning approach is ideally suited for

parallel implementation. The authors are pursuing this avenue prior to integration of the algorithm with the CHT solver. This concludes the example section.

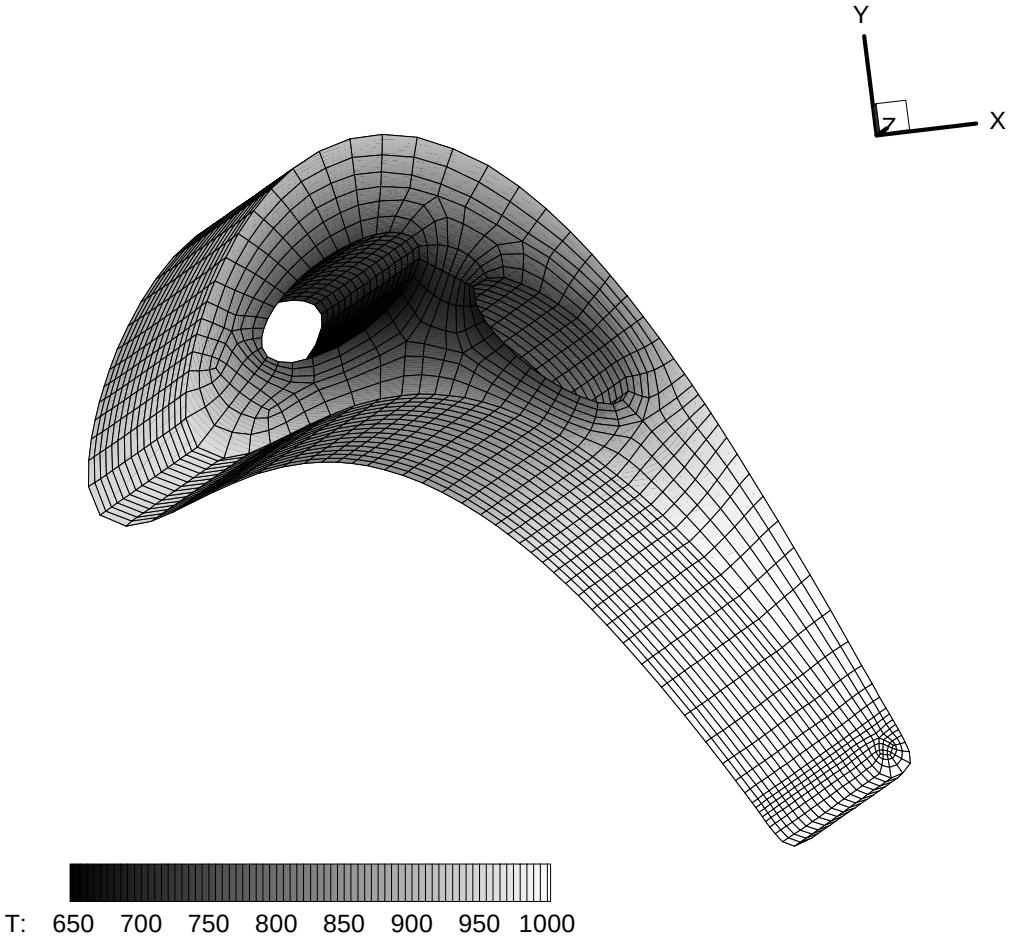

Figure 26. Converged surface temperature distribution (K)

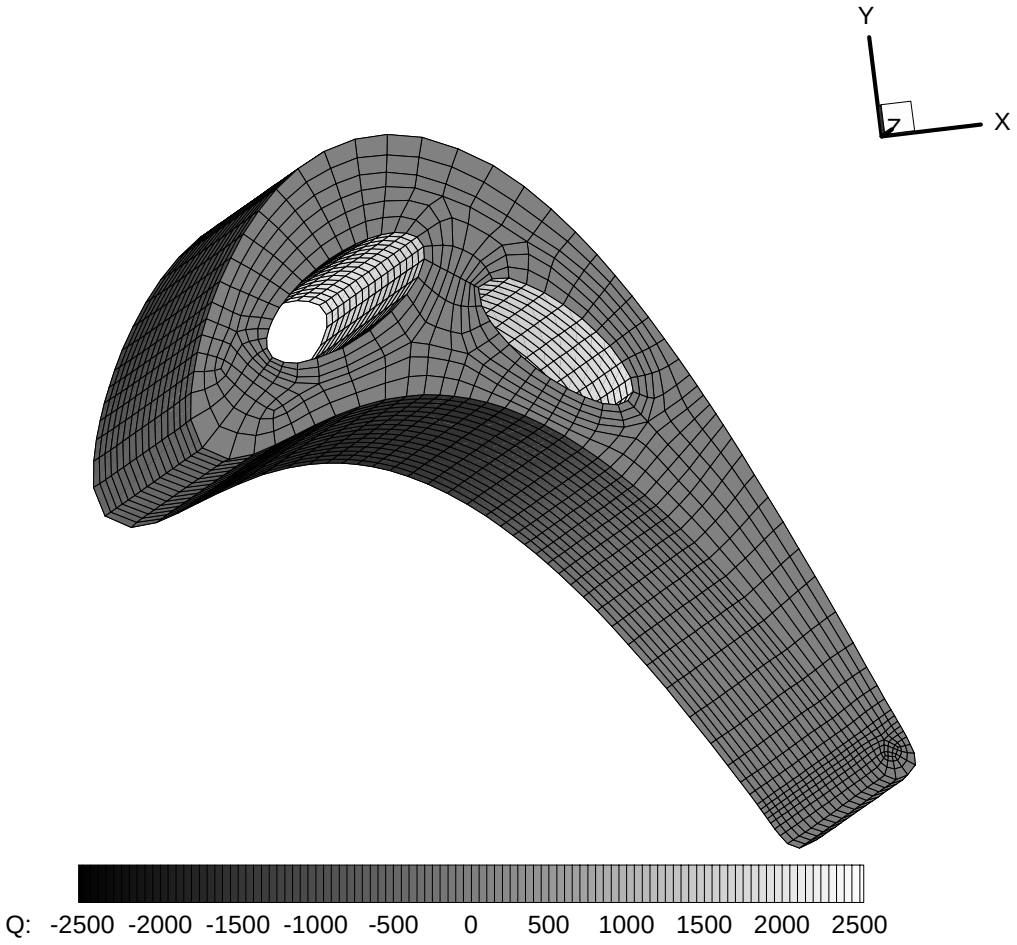

Figure 27. Converged surface heat flux distribution $(\frac{1}{100}W/m^2K)$

6 Conclusions

A combined BEM/FVM approach using the TFFB conjugate method has been implemented in a 3-D context to model CHT in cooled turbine blades. As a boundary-only grid is used by the BEM, the computational time for the heat conduction analysis is insignificant compared to the time used for the NS analysis. The proposed method produces realistic results without using arbitrary assumptions for the thermal condition at the conductor surface. Results from a CHT numerical simulation of a 3-D film-cooled blade section are presented and are compared with those obtained from the standard approach of a two temperature model. A significant difference in the level and distribution of the metal temperatures is found between the

two models. These differences have severe implications in materials design and subsequent thermal stress analysis of the blade carried out using these metal temperatures. In practice, turbomachinery components such as modern cooled turbine blades which often contain several hundred film cooling holes and intricate internal serpentine cooling passages with complex convective enhancement configurations such as turbulating trip strips. This poses a real computational challenge to BEM modeling. The subsectioning iterative approach outlined in this report thus offers a promising technique to address this problem.

Future Work

We are in the process of building a PC-based cluster running under Windows. We are extending the sub-structure code under MPI and MPI-2 parallel protocols. Testing and fine tuning of the code will be undertaken in the course of the next year. We will implement a GMRES iterative solver to speed up computations at the sub-section level of the current code. This work is expected to continue into January. We will also begin to develop a 3D parallel multipole BEM fast solver to be run with a GMRES pre-conditioned non-symmetric solver. This phase of the project will be undertaken over the next two years.

References

[1] Kassab, A.J. and Aliabadi, M.H. (eds.), *Advances in Boundary Elements: Coupled Field Problems,* Computational Mechanics, Boston, 2001.

[2] Heidmann, J., Rigby, D., and Ameri, A., A Three-Dimensional Coupled External/Internal Simulation of a Film-Cooled Turbine Vane, *ASME Journal of Turbomachinery*, Vol. 122, pp. 348-359, 2002.

[3] Comini, G., Saro, O. and Manzan, M., A Physical Approach to Finite Element Modeling of Coupled Conduction and Convection, *Numerical Heat Transfer, Part. B.*, Vol. 24, pp. 243-261, 1993.

[4] Shyy, W. and Burke, J., Study of Iterative Characteristics of Convective Diffusive and Conjugate Heat Transfer Problems, *Numerical Heat Transfer, Part. B.*, Vol. 26, pp. 21-37, 1994.

[5] Patankar, S.V., A Numerical Method for Conduction in Composite Materials, Flow in Irregular Geometries and Conjugate Heat Transfer, *Proc. 6th. Int. Heat Transfer Conf.*, NRC Canada, and Hemisphere Pub. Co., New York, Vol. 3, pp. 297-302, 1978.

[6] Kao, K.H., and Liou, M.S., Application of Chimera/Unstructured Hybrid grids for Conjugate Heat Transfer, *AIAA Journal*, Vol. 35, No. 9, pp. 1472-1478, 1997.

[7] Hahn, Z., Dennis, B., and Dulikravich, G., Simultaneous Prediction of External Flow-field and Temperature in Internally Cooled 3-D Turbine Blade Material, *IGTI Paper 2000-GT-253*, 2000.

[8] Bohn, D., Becker, V., Kusterer, K., Otsuki, Y., Sugimoto, T., and Tanaka, R., 3-D Internal Conjugate Calculations of a Convectively Cooled Turbine Blade with Serpentine-Shaped Ribbed Channels, *IGTI Paper 99-GT-220*, 1999.

[9] Bohn, D.E., Becker, V.J., and Rungen, A.U., Experimental and Numerical Conjugate Flow and Heat Transfer Investigation of a Shower-Head Cooled Turbine Guide Vane, ASME Paper 97-GT-15.

[10] Tayala, S.S., Rajadas, J.N., and Chattopadyay, A., Multidisciplinary Optimization for Gas Turbine Airfoil Design, *Inverse Problems in Engineering*, Vol. 8, No. 3, pp. 283- 307, 2000.

[11] Hassan, B., Kuntz, D. and Potter, D.L., Coupled Fluid/Thermal Prediction of Ablating Hypersonic Vehicles, *AIAA Paper 98-0168*, 1998.

[12] Brown, S.A., Displacement Extrapolations for CFD+CSM Aeroelastic Analysis, *AIAA Paper 97-1090*, 1997.

[13] Dowell, E., and Hall, K.C., Modeling of Fluid Structure Interaction, *Annual Review of Fluid Mechanics*, Vol. 33, pp. 445-490, 2001.

[14] Li, H. and Kassab, A.J., Numerical Prediction of Fluid Flow and Heat Transfer in Turbine Blades with Internal Cooling, *AIAA/ASME Paper 94-2933.*

[15] Li, H. and Kassab, A.J., A Coupled FVM/BEM Solution to Conjugate Heat Transfer in Turbine Blades, *AIAA Paper 94-1981*.

[16] Ye, R., Kassab, A.J., and Li, H.J., FVM/BEM Approach for the Solution of Nonlinear Conjugate Heat Transfer Problems, *Proc. BEM 20*, Kassab, A.J., Brebbia, C.A., and Chopra, M.B., (eds.), Orlando, Florida, August 19-21, 1998, pp. 679-689.

[17] Program Development Corporation, GridPro^{TM}/az3000-User's guide and Reference Manual, White Plains, New York, 1997.

[18] He, M., Kassab, A.J., Bishop, P.J., and Minardi, A., A Coupled FDM/BEM Iterative Solution for the Conjugate Heat Transfer Problem in Thick-Walled Channels: Constant Temperature Imposed at the Outer Channel Wall, *Engineering Analysis*, Vol. 15, No. 1, pp. 43-50, 1995.

[19] He, M., Bishop, P., Kassab, A.J., and Minardi, A., A Coupled FDM/BEM solution for the Conjugate Heat Transfer Problem, *Numerical Heat Transfer, Part B: Fundamentals,* Vol. 28, No. 2, pp. 139-154, 1995.

[20] Kontinos, D., Coupled Thermal Analysis Method with Application to Metallic Thermal Protection Panels, *AIAA Journal of Thermophysics and Heat Transfer,* Vol. 11, No. 2, pp. 173-181, 1997.

[21] Rahaim, C.P., Kassab, A.J. and Cavalleri, R., A Coupled Dual Reciprocity Boundary Element/Finite Volume Method for Transient Conjugate Heat Transfer, *AIAA Journal of Thermophysics and Heat Transfer*, Vol. 14, No. 1, pp. 27-38, 2000.

[22] Rahaim, C., Cavalleri, R.J. and Kassab, A.J., Computational Code For Conjugate Heat Transfer Problems: An Experimental Validation Effort, *AIAA Paper 97-2487,* 1997.

[23] Partridge, P.W., Brebbia, C.A. and Wrobel, L.C., *The Dual Reciprocity Boundary Element Method*, Computational Mechanics Publications, Southampton, 1992.

[24] E. Divo, E. Steinthorsson, A. J. Kassab, and R. Bialecki, An iterative BEM/FVM protocol for steady-state multi-dimensional conjugate heat transfer in compressible flows, *Engineering Analysis with Boundary Elements*, Volume 26, No. 5, pp. 447-454, 2002.

[25] Kassab, A., Divo, E., Heidmann, J., Steinthorsson, E., and Rodriguez, F., "BEM/FVM Conjugate Heat Transfer Analysis of a Three-Dimensional Film Cooled Turbine Blade," *International Journal for Numeical Methods in Heat and Fluid Flow*, (in review).

[26] Kassab, A.J. and Nordlund, R.S., "Addressing the Corner Problem in the BEM Solution of Heat Conduction Problems," *Communications in Numerical Methods in Engineering*, Vol. 10, 1994, pp. 385-392.

[27] Kane, J., *Boundary Element Analysis in Engineering and Continuum Mechanics*, Prentice-Hall, Englewood Cliffs, New Jersey, 1994.

[28] Turkel, E., Preconditioned Methods for Solving the Incompressible and Low-Speed Compressible Equations, *Journal of Computational Physics*, Vol. 72, No. 2, pp. 277-298, 1987.

[29] Turkel, E., Review of Preconditioning Methods for Fluid Dynamics, *Applied Numerical Mathematics*, Vol. 12, pp. 257-284, 1993.

[30] Wilcox, D.C., Turbulence Modeling for CFD, DCW Industries, La Canada, California, 1993.

[31] Wilcox, D.C., Simulation of transition with a two-equation turbulence model, *AIAA Journal*, Vol. 32, No. 2, pp. 247-255, 1994.

[32] Menter, F. R., Zonal Two-Equation k-ω Turbulence Models for Aerodynamic Flows, *AIAA Paper 93-2906*, 1993.

[33] Chima, R. V., A k-ω Turbulence Model for Quasi-Three-Dimensional Turbomachinery Flows, *NASA TM-107051*, 1996.

[34] Azevedo, J.P.S. and Wrobel, L.C., Non-Linear Heat Conduction in Composite Bodies: A Boundary Element Formulation, *International Journal for Numerical Methods in Engineering*, Vol. 26, pp. 19-38, 1988.

[35] Bialecki, R. and Nhalik, R., Solving Nonlinear Steady State Potential Problems in Inhomogeneous Bodies Using the Boundary Element Method, *Numerical Heat Transfer, Part B*, Vol. 15, pp. 79-96, 1989.

[36] F. Rodriguez, E. Divo, and A.J. Kassab,"A Strategy for BEM Modeling of Large-Scale Three Dimensional Heat Transfer Problems," Kassab, A.J., Nicholson, D.W., and Ionescu, I.(eds.), *Proceedings of SECTAM XXI, Recent Advances in Theoretical and Applied Mechanics*, Orlando, Florida, May 19-21, 2002, pp. 645-654.

[37] Kassab, A.J. and Wrobel, L.C., Boundary Element Methods in Heat Conduction, Chapter 5 in *Recent Advances in Numerical Heat Transfer,* W.J. Mincowycz and E. M. Sparrow, (eds.), Vol. 2, Taylor and Francis, New York, 2000, pp. 143-188.

[38] Steinthorsson, E., Ameri, A., and Rigby, D., *LeRC-HT -The NASA Lewis Research Center General Multi-Block Navier-Stokes Convective Heat Transfer Code,* (unpublished).

[39] Steinthorsson, E., Liou, M.-S, and Povinelli, L.A., Development of an Explicit Multi-block/Multigrid Flow Solver for Viscous Flows in Complex Geometries, *AIAA Paper 93-2380,* 1993.

[40] Rigby, D. L., Ameri, A. A., and Steinthorsson, E., Numerical Prediction of Heat Transfer in a Channel with Ribs and Bleed, *ASME Paper 97-GT-431*, 1997.

[41] Ameri, A. A., Steinthorsson, E., and Rigby, D. L., Effect of Squealer Tip on Rotor Heat Transfer and Efficiency, ASME Paper 97-GT-128, 1997

[42] Jameson,A., Schmidt, W., and Turkel, E., Numerical simulation of the Euler equations by the finite volume methods using Runge-Kutta time stepping schemes, *AIAA Paper 81-1259*.

[43] Schlichting, H., Boundary Layer Theory, McGraw-Hill, New York, 7th edition, pp. 312-313, 1979.

[44] Brebbia, C.A., Telles, J.C.F. and Wrobel, L.C., *Boundary Element Techniques*, Springer-Verlag, Berlin, 1984.

[45] Brebbia, C.A. and Dominguez, J., *Boundary Elements: An Introductory Course*, Computational Mechanics Pub., Southampton and McGraw-Hill, New York, 1989.

[46] Banerjee, P.K., *Boundary Element Method*, MacGraw Hill Book, Co, New York, 1994.

[47] Liggett, J.A., and Liu, P. L-F, *The Boundary Integral Equation Method for Porous Media Flow*, *Allen* & Unwin, Boston, 1983.

[48] Morse, P.M. and Feshbach, H., *Methods of Theoretical Physics*, McGraw-Hill, New York, 1953.

[49] Kellogg, O.D., *Foundations of Potential Theory*, Dover, New York, 1953.

[50] Bialecki, R., Ostrowski, Z., Kassab, A., Qi, Y., and Sciubba, E., Coupling Finite Element and Boundary Element Solutions, *Proc. of the 2001 European Conference on Computational Mechanics*, June 26-29, 2001, Cracow, Poland.

[51] Bialecki, R.A., Merkel, M., Mews, H., and Kuhn, G., In-and Out-Of-Core BEM Equation Solver with Parallel and Nonlinear Options, *International Journal for Numerical Methods in Engineering*, Vol. 39, pp. 4215-4242, 1996.

[52] Kane, J.H., Kashava-Kumar, B.L., and Saigal, S., An Arbitrary Condensing, Non-Condensing Strategy for Large Scale, Multi-zone Boundary Element Analysis, *Computer Methods in Applied Mechanics and Engineering*, Vol. 79, pp. 219-244, 1990.

[53] Greengard, L. and Strain, J., A Fast Algorithm for the Evaluation of Heat Potentials, *Communications in Pure and Applied Mathematics*, Vol. 43, pp. 949-963, 1990.

[54] Hackbush, W. and Nowak, Z. P., On the Fast Multiplication in the Boundary Element Method by Panel Clustering, *Numerische Mathematik*, Vol. 54, pp. 463-491, 1989.

[55] Gomez, J.E. and Power, H., A Multipole Direct and Indirect BEM for 2-D Cavity Flows at Low Reynolds Number, *Engineering Analysis with Boundary Elements*, Vol. 19, No.1, pp. 17-31, 1997

[56] Bucher, H. and Wrobel, L.C., A Novel Approach to Applying Wavelet Transforms in Boundary Element Method, *Advances in Boundary Element Techniques*, II, Denda, M., Aliabadi, M.H., and Charafi, A., (eds.), Hogaar Press, Switzerland, pp. 3-11, 2000.

[57] Divo, E., Rodriguez, F., and Kassab, A.J., A Strategy for Linear and Nonlinear Three Dimensional BEM Heat Conduction Models, *Numerical Heat Transfer* (in review).

[58] Abramowitz, M. and Stegun, I., Handbook of Mathematical Functions, Dover Publications, New York, 1965.

[59] Ralston, A. and Rabinowitz, P., A First Course in Numerical Analysis, Mc Graw Hill Book Co., New York, 1978.

Appendix: Numerical Evaluation of the Influence Coefficients

The process is most readily illustrated by considering constant elements. In the constant element, which is a subparametric element, the field variables, T and q, are modeled as constant across each element while the geometry is represented locally as bilinear planes. Figure A.1. below shows a typical constant boundary element along with its transformed representation in the local $\eta - \zeta$ coordinate system.

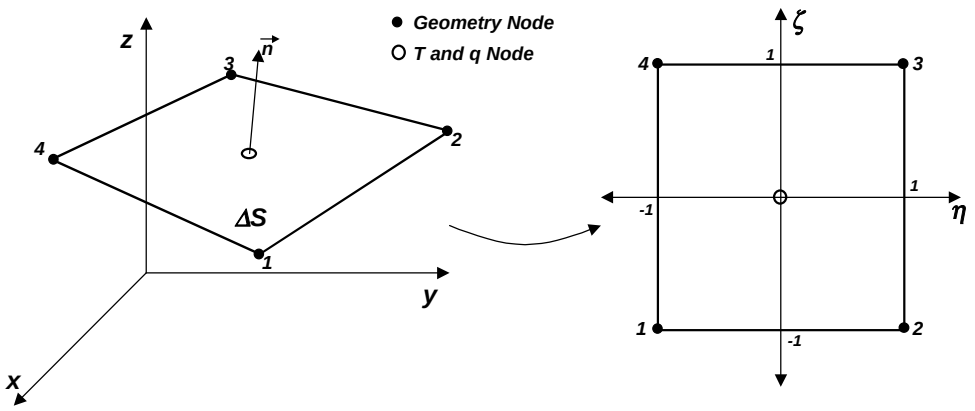

Figure A.1. Bilinear subparametric boundary element.

Notice that the geometric nodal locations of the element are ordered counterclockwise such that the normal vector always points outwards from the domain of the problem. The global coordinate system (x, y, z) is transformed into a local coordinate system (η, ζ) using the bilinear shape functions as given in Eqn. (15). However, the temperature and heat flux are modeled as constant with the node located at the geometric center of the boundary element, thus

$$T_j(\eta, \zeta) = T_j \quad \text{and} \quad q_j(\eta, \zeta) = q_j \tag{A.1}$$

Clearly, the temperature and heat flux are discontinuous at the element interfaces. Thus, a constant element is termed discontinuous. Introducing the above discretization in the BIE and noting that $NPE = 1$, and collocating the discretized BIE at each of the boundary nodes ξ_i there results

$$C(\xi_i)\, T(\xi_i) + \sum_{j=1}^{N} H_{ij}\, T_j = \sum_{j=1}^{N} G_{ij}\, q_j \tag{A.2}$$

where the influence coefficients H_{ij} and G_{ij} are defined as

$$H_{ij} = \oint_{\Delta S_j} q^*(x_j, \xi_i) dS(x) \tag{A.3}$$
$$G_{ij} = \oint_{\Delta S_j} T^*(x_j, \xi_i) dS(x)$$

These are evaluated numerically using Gauss-Legendre quadratures with an adaptive scheme to be discussed shortly. Although very simple in implementation, use of the above constant element formulation does not lead to satisfactory results in many cases, and these are discussed purely for illustration. Introducing the definition of bilinear representation of the geometry into the constant element influence coefficient definition, the constant element influence coefficient integrals are explicitly,

$$H_{ij} = \int_{-1}^{1}\int_{-1}^{1} q^*(x(\eta,\zeta), \xi_i) J_j(\eta,\zeta) d\eta\, d\zeta \tag{A.4}$$
$$G_{ij} = \int_{-1}^{1}\int_{-1}^{1} T^*(x(\eta,\zeta), \xi_i) J_j(\eta,\zeta) d\eta\, d\zeta$$

The Jacobian of the transformation over the j-th element, $J_j(\eta,\zeta)$ is

$$J_j(\eta,\zeta) = \sqrt{g_{\eta\eta} g_{\zeta\zeta} - g_{\eta\zeta}^2} \tag{A.5}$$

where $g_{\eta\eta}$, $g_{\zeta\zeta}$, and $g_{\eta\zeta}$ are the components of the metric tensor defined as,

$$
\begin{aligned}
g_{\eta\eta} &= \left(\frac{\partial x}{\partial \eta}\right)^2 + \left(\frac{\partial y}{\partial \eta}\right)^2 + \left(\frac{\partial z}{\partial \eta}\right)^2 \\
g_{\zeta\zeta} &= \left(\frac{\partial x}{\partial \zeta}\right)^2 + \left(\frac{\partial y}{\partial \zeta}\right)^2 + \left(\frac{\partial z}{\partial \zeta}\right)^2 \\
g_{\eta\zeta} &= \left(\frac{\partial x}{\partial \eta}\frac{\partial x}{\partial \zeta}\right) + \left(\frac{\partial y}{\partial \eta}\frac{\partial y}{\partial \zeta}\right) + \left(\frac{\partial z}{\partial \eta}\frac{\partial z}{\partial \zeta}\right)
\end{aligned}
\tag{A.6}
$$

The metrics $\frac{\partial x}{\partial \eta}$, $\frac{\partial x}{\partial \zeta}$, $\frac{\partial y}{\partial \eta}$, $\frac{\partial y}{\partial \zeta}$, $\frac{\partial z}{\partial \eta}$, and $\frac{\partial z}{\partial \zeta}$ are readily found by differentiation of $x_j(\eta,\, \zeta)$, $y_j(\eta,\, \zeta)$, and $z_j(\eta,\, \zeta)$ in Eqn. (15). Introducing the metrics into the Jacobian and simplifying leads to,

$$
J_j(\eta, \zeta) = \sqrt{\left(\frac{\partial y}{\partial \eta}\frac{\partial z}{\partial \zeta} - \frac{\partial z}{\partial \eta}\frac{\partial y}{\partial \zeta}\right)^2 + \left(\frac{\partial z}{\partial \eta}\frac{\partial x}{\partial \zeta} - \frac{\partial x}{\partial \eta}\frac{\partial z}{\partial \zeta}\right)^2 + \left(\frac{\partial x}{\partial \eta}\frac{\partial y}{\partial \zeta} - \frac{\partial y}{\partial \eta}\frac{\partial x}{\partial \zeta}\right)^2}
\tag{A.7}
$$

In the expression for $q^*(x,\, \xi_i)$ there arises the need to evaluate the outward-drawn normal $\widehat{n}$, as by definition

$$
q^*(x,\, \xi_i) = -k\frac{\partial\, T^*(x,\, \xi_i)}{\partial\, n} = -k\nabla q^*(x,\, \xi_i)\cdot \widehat{n}
\tag{A.8}
$$

The components of the unit vector on each elements can be easily computed using,

$$
\begin{aligned}
n_x &= \left(\frac{\partial y}{\partial \eta}\frac{\partial z}{\partial \zeta} - \frac{\partial z}{\partial \eta}\frac{\partial y}{\partial \zeta}\right)/J_j(\eta, \zeta) \\
n_y &= \left(\frac{\partial z}{\partial \eta}\frac{\partial x}{\partial \zeta} - \frac{\partial x}{\partial \eta}\frac{\partial z}{\partial \zeta}\right)/J_j(\eta, \zeta) \\
n_z &= \left(\frac{\partial x}{\partial \eta}\frac{\partial y}{\partial \zeta} - \frac{\partial y}{\partial \eta}\frac{\partial x}{\partial \zeta}\right)/J_j(\eta, \zeta)
\end{aligned}
\tag{A.9}
$$

The numerical integration process necessary to obtain the influence coefficients is performed by double Gaussian quadratures (Gauss-Legendre specifically) simultaneously along the two local axis η and ζ, leading to the following form,

$$H_{ij} = \sum_{n=1}^{NG} \sum_{m=1}^{NG} W_n W_m q^*(x_j(\eta_{nm}, \zeta_{nm}), \xi_i) J_j(\eta_{nm}, \zeta_{nm}) \tag{A.10}$$

$$G_{ij} = \sum_{n=1}^{NG} \sum_{m=1}^{NG} W_n W_m T^*(x_j(\eta_{nm}, \zeta_{nm}), \xi_i) J_j(\eta_{nm}, \zeta_{nm})$$

where *NG* is the number of Gaussian points or order of integration employed, η_{nm} and ζ_{nm} are the locations of the Gaussian quadrature points (zeroes of the appropriate Legendre polynomials), and W_n and W_m are the quadrature weights [58,59].

The number of Gaussian points employed can be adapted to every integral depending on the variability of the integrand. The influence coefficients G are inversely proportional to the Euclidean distance between the field or integration point x and the collocation point ξ_i, and the influence factors H are inversely proportional to the square of the Euclidean distance between the field or integration point and the collocation point ξ_i. Therefore, as the collocation point ξ_i is positioned closer to the integration element, the variability of the integrand increases requiring an increase in the number of Gaussian points, *NG*, for the integral approximation to provide a similar level of accuracy. Hence, a simple distance rule can be heuristically employed to change the number of Gaussian points depending on how far the collocation point is to the integration element. For non-singular elements, the following ratio of lengths is computed prior to integration

$$r_c = \frac{r_{ij-max}}{r_{ij-min}} \tag{A.11}$$

where r_{ij} is measured from the collocation point ξ_i to 49 (7x7 equidistant) locations along the integration element j. The following is a table of heuristic quadrature and adaption rules determined by experience that are adopted in the 3-D BEM code:

Table A.1 Gauss and adaption rules used in the BEM code.

r_c Range	# of Integration Cells	Gaussian Points
$1 < r_c \leq 1.2$	1	9 (3 x 3)
$1.2 < r_c \leq 1.5$	1	25 (5 x 5)
$1.5 < r_c \leq 2.0$	1	49 (7 x7)
$2.0 < r_c \leq 3.0$	1	100 (10 x 10)
$3.0 < r_c \leq 5.0$	1	225 (15 x 15)
$5.0 < r_c \leq 7.5$	1	400 (20 x 20)
$7.5 < r_c \leq 10$	1	625 (25 x 25)
$10 < r_c \leq 25$	4 (2 x 2)	4 x 900 (30 x 30)
$25 < r_c \leq 50$	9 (3 x 3)	9 x 900 (30 x 30)
$50 < r_c \leq 100$	16 (4 x 4)	16 x900 (30 x 30)
$100 < r_c \leq 200$	25 (5 x 5)	25 x 900 (30 x 30)
$200 < r_c \leq 500$	36 (6 x 6)	36 x 900 (30 x 30)
$r_c > 500$	64 (8 x 8)	64 x 900 (30 x 30)

However, simply increasing the number of Gaussian integration points is in some cases not enough to obtain an accurate approximation to the integral. This is precisely the case when the collocation point ξ_i is extremely close to the integration element. In such cases a subsegmentation of the element is required and can be performed in a similar fashion as to the increase of Gaussian points, that is, the closer the collocation point is to the element, the more subdivisions are made to the element with a fixed number of Gaussian points for each subelement.

The particular case in which the collocation point ξ_i is located over the integration element must be treated with caution. For this case the integrand becomes singular lacking an accurate integral approximation through a regular Gaussian rule. Even though the integral for the influence factor H_{ii} is strongly singular because its integrand is inversely proportional to the distance squared $(1/r^2)$, this integral need not be computed directly unless regularized, and instead it can be evaluated using the equipotential relation by summing the off-diagonal terms [44-46], that is

$$H_{ii} = -\sum_{j=1,\, j\neq i}^{N} H_{ij} \tag{A.12}$$

The integral for the influence coefficient G_{ii} is however weakly singular because its integrand is inversely proportional to the distance $(1/r)$, and can be accurately computed through a transformation of the local coordinate system which effectively clusters the Gauss points. Figure A.2 shows the primary subsegmentation of the singular element. Twelve quadrilateral subdivisions have been made to the singular subparametric boundary element in Fig. A.2. The shaded area $''0''$ corresponds to the singular portion of the element that is to be transformed into a local polar coordinate system.

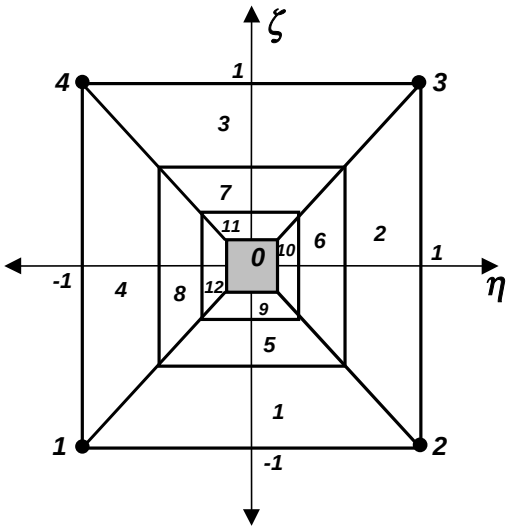

Figure A.2. Subsegmentation of singular bilinear subparametric boundary element.

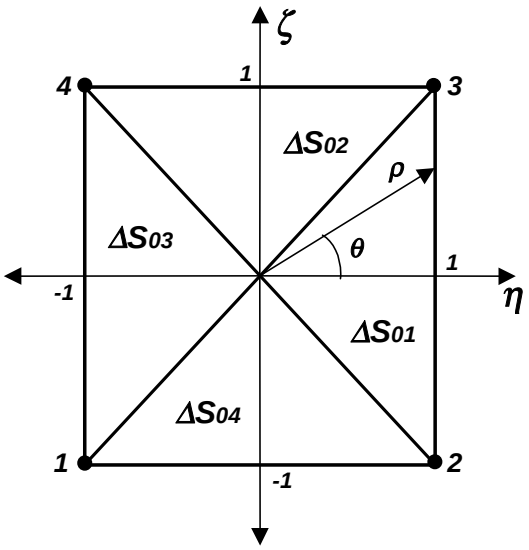

Figure A.3. Polar coordinate transformation of the area "0" of the singular boundary element.

The shaded area of the singular element is fit into a new local system (η, ζ) and subdivided into four triangular subelements. Each of the subelements is transformed into a new local polar coordinate system (ρ, θ) where,

$$\begin{aligned} \eta &= \rho \cos\theta \\ \zeta &= \rho \sin\theta \end{aligned} \tag{A.13}$$

therefore, the factor G_{ii}^{0} which corresponds to the integral over the shaded area $''0''$ is comprised of four integrals (G_{ii}^{01}, G_{ii}^{02}, G_{ii}^{03}, and G_{ii}^{04}) as,

$$G_{ii}^{01} = \int_{-\frac{\pi}{4}}^{\frac{\pi}{4}} \int_{0}^{\frac{1}{\cos\theta}} T^{*}(x_i(\eta,\zeta),\xi_i) J_i(\eta,\zeta) \rho \, d\rho \, d\theta \tag{A.14}$$

$$G_{ii}^{02} = \int_{\frac{\pi}{4}}^{\frac{3\pi}{4}} \int_{0}^{\frac{1}{\sin\theta}} T^{*}(x_i(\eta,\zeta),\xi_i) J_i(\eta,\zeta) \rho \, d\rho \, d\theta$$

$$G_{ii}^{03} = \int_{\frac{3\pi}{4}}^{\frac{5\pi}{4}} \int_{0}^{\frac{1}{\cos\theta}} T^{*}(x_i(\eta,\zeta),\xi_i) J_i(\eta,\zeta) \rho \, d\rho \, d\theta$$

$$G_{ii}^{04} = \int_{\frac{5\pi}{4}}^{\frac{7\pi}{4}} \int_{0}^{\frac{1}{\sin\theta}} T^{*}(x_i(\eta,\zeta),\xi_i) J_i(\eta,\zeta) \rho \, d\rho \, d\theta$$

Notice that the transformation of the differential area introduced the variable ρ to the integrand which relaxes the singularity of the fundamental solution $T^*(x_j(\eta,\zeta),\xi_i)$. In addition, an extra transformation is necessary to fit the limits of integration into the $(-1,1)$ range such that,

$$\begin{aligned}
\rho_1 &= \frac{s+1}{2cos\,\theta_1} \;\;,\;\; \theta_1 = \frac{\pi}{4}t \\
\rho_2 &= \frac{s+1}{2sin\,\theta_2} \;\;,\;\; \theta_2 = \frac{\pi}{4}(t+2) \\
\rho_3 &= \frac{s+1}{2cos\,\theta_3} \;\;,\;\; \theta_3 = \frac{\pi}{4}(t+4) \\
\rho_4 &= \frac{s+1}{2sin\,\theta_4} \;\;,\;\; \theta_4 = \frac{\pi}{4}(t+6)
\end{aligned} \tag{A.15}$$

where the subindeces of the coordinates ρ and θ correspond to the transformation for the particular integral term G_{ii}^{01}, G_{ii}^{02}, G_{ii}^{03}, and G_{ii}^{04}. Therefore, the influence coefficient subintegrals are transformed into,

$$\begin{aligned}
G_{ii}^{01} &= \int_{-1}^{1}\int_{-1}^{1} T^*(x_i(\eta,\zeta),\xi_i) J_i(\eta,\zeta) \frac{\pi\rho_1}{8cos\,\theta_1}\, ds\, dt \\
G_{ii}^{02} &= \int_{-1}^{1}\int_{-1}^{1} T^*(x_i(\eta,\zeta),\xi_i) J_i(\eta,\zeta) \frac{\pi\rho_2}{8sin\,\theta_2}\, ds\, dt \\
G_{ii}^{03} &= \int_{-1}^{1}\int_{-1}^{1} T^*(x_i(\eta,\zeta),\xi_i) J_i(\eta,\zeta) \frac{\pi\rho_3}{8cos\,\theta_3}\, ds\, dt \\
G_{ii}^{04} &= \int_{-1}^{1}\int_{-1}^{1} T^*(x_i(\eta,\zeta),\xi_i) J_i(\eta,\zeta) \frac{\pi\rho_4}{8sin\,\theta_4}\, ds\, dt
\end{aligned} \tag{A.16}$$

which can be solved numerically by the use of Gaussian integration and through the corresponding transformations detailed in the previous relations. Each triangle is integrated using a 100 (10 x 10) Gaussian point rule distributed in the transformed $r-\theta$ system. Each of the remaining 12 cells that do not contain singularities are integrated using a 900 (30 x 30) Guassian point rule.

When dealing with isoparametric bilinear elements, the procedure of evaluation of the element influence coefficients H_{ij}^k and G_{ij}^k is the same, except that the shape functions $M^k(\eta,\zeta)$,

$k = 1...4$, appear multiplying each of the integrands of the influence coefficients. That is for instance,

$$G_{ij}^k = \int_{-1}^{1}\int_{-1}^{1} T^*(x_j(\eta,\zeta),\xi_i) M^k(\eta,\zeta) J_j(\eta,\zeta) d\eta\, d\zeta \tag{A.17}$$

$$G_{ij}^k = \sum_{n=1}^{NG}\sum_{m=1}^{NG} W_n W_m T^*(x_j(\eta_{nm},\zeta_{nm}),\xi_i) M^k(\eta_{nm},\zeta_{nm}) J_j(\eta_{nm},\zeta_{nm})$$

where the subscript $i = 1...4N$ refers to the collocation point ξ_i which is positioned at all four offset nodal locations of each element. The subscript $j = 1...N$ refers to the integration element and the subscript $k = 1...4$ corresponds to each of the shape functions $M^k(\eta,\zeta)$ in the integrand.

The subsegmentation described for the G_{ii} influence coefficient in the subparametric element is extended to the case of discontinuous isoparametric elements by performing a non-symmetric subsegmentation of the element i depending on the location of the collocation point ξ_i on the boundary element, see Fig. (A.4).

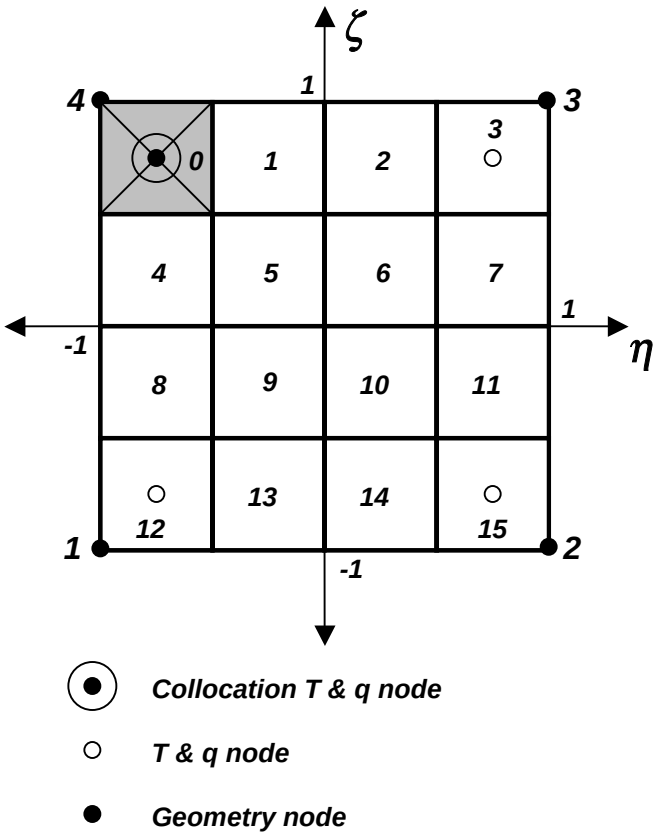

Figure A.4. Subsegmentation of singular bilinear isoparametric boundary element.

REPORT DOCUMENTATION PAGE

Form Approved
OMB No. 0704-0188

1. AGENCY USE ONLY (*Leave blank*)	2. REPORT DATE	3. REPORT TYPE AND DATES COVERED
	April 2003	Annual Contractor Report—October 1, 2001–October 2, 2002

4. TITLE AND SUBTITLE

Glenn-HT/BEM Conjugate Heat Transfer Solver for Large-Scale Turbomachinery Models

5. FUNDING NUMBERS

WU–708–87–23–00
NAG3–2691

6. AUTHOR(S)

E. Divo, E. Steinthorsson, F. Rodriguez, A.J. Kassab and J.S. Kapat

7. PERFORMING ORGANIZATION NAME(S) AND ADDRESS(ES)

University of Central Florida
Mechanical, Materials, and Aerospace Engineering Department
P.O. Box 160001
Orlando, Florida 32816

8. PERFORMING ORGANIZATION REPORT NUMBER

E–13798

9. SPONSORING/MONITORING AGENCY NAME(S) AND ADDRESS(ES)

National Aeronautics and Space Administration
Washington, DC 20546–0001

10. SPONSORING/MONITORING AGENCY REPORT NUMBER

NASA CR—2003-212195

11. SUPPLEMENTARY NOTES

Project Manager, James D. Heidmann, Turbomachinery and Propulsion Systems Division, NASA Glenn Research Center, organization code 5820, 216–433–3604.

12a. DISTRIBUTION/AVAILABILITY STATEMENT

Unclassified - Unlimited
Subject Categories: 01 and 07 Distribution: Nonstandard

Available electronically at http://gltrs.grc.nasa.gov

This publication is available from the NASA Center for AeroSpace Information, 301–621–0390.

12b. DISTRIBUTION CODE

13. ABSTRACT ***(Maximum 200 words)***

A coupled Boundary Element/Finite Volume Method temperature-forward/flux-hack algorithm is developed for conjugate heat transfer (CHT) applications. A loosely coupled strategy is adopted with each field solution providing boundary conditions for the other in an iteration seeking continuity of temperature and heat flux at the fluid-solid interface. The NASA Glenn Navier-Stokes code Glenn-HT is coupled to a 3-D BEM steady state heat conduction code developed at the University of Central Florida. Results from CHT simulation of a 3-D film-cooled blade section are presented and compared with those computed by a two-temperature approach. Also presented are current developments of an iterative domain decomposition strategy accommodating large numbers of unknowns in the BEM. The blade is artificially sub-sectioned in the span-wise direction, 3-D BEM solutions are obtained in the subdomains, and interface temperatures are averaged symmetrically when the flux is updated while the fluxes are averaged anti-symmetrically to maintain continuity of heat flux when the temperatures are updated. An initial guess for interface temperatures uses a physically-based 1-D conduction argument to provide an effective starting point and significantly reduce iteration. 2-D and 3-D results show the process converges efficiently and offers substantial computational and storage savings. Future developments include a parallel multi-grid implementation of the approach under MPI for computation on PC clusters.

14. SUBJECT TERMS

Conjugate heat transfer; Boundary elements; Coupled finite volume; Boundary element method

15. NUMBER OF PAGES

70

16. PRICE CODE

17. SECURITY CLASSIFICATION OF REPORT	18. SECURITY CLASSIFICATION OF THIS PAGE	19. SECURITY CLASSIFICATION OF ABSTRACT	20. LIMITATION OF ABSTRACT
Unclassified	Unclassified	Unclassified	